Energy Engineering

Tech Science Press

Doi:10.32604/ee.2025.073028

ARTICLE

Low-Frequency Oscillation Analysis of Grid-Forming Energy Storage Converters Based on a Multi-Damping Path Model

Qiang Liu[1], Yongqiang Zhou[1], Chaoyang Lu[2], Zhen Yan[1], Gangui Yan[2], Cheng Yang[2,*] and Yupeng Wang[2]

[1]Xingtai Power Supply Branch, State Grid Hebei Electric Power Co., Ltd., Xingtai, 054001, China
[2]Key Laboratory of Modern Power System Simulation and Control & Renewable Energy Technology, Ministry of Education (Northeast Electric Power University), Jilin, 132012, China

*Corresponding Author: Cheng Yang. Email: yangcheng199368@163.com

Received: 09 September 2025; Accepted: 21 October 2025; Published: 06 August 2026

ABSTRACT: The increasing proportion of power generated by new energy has meant that grid-forming energy storage has become a key method for improving power grid flexibility. However, the small disturbance stability problem has become an important challenge. The issue is that grid-forming energy storage is prone to low-frequency oscillation under strong grid conditions. Therefore, this study proposes a multi damping torque model to analyze the small signal stability of grid-forming energy storage converters. The impact of grid strength, operating conditions, and control parameters on the damping characteristics of the low-frequency oscillation by the system was quantitatively evaluated. The results revealed the mechanism underlying the low-frequency oscillation associated with grid-forming energy storage under strong grid conditions and key factors controlling the low-frequency oscillation. The results also provide theoretical guidance for the tuning of grid-forming energy storage control parameters. The accuracy of the multi damping torque model and theoretical analysis were verified using the electromagnetic simulation results.

KEYWORDS: Multi-damping path; grid-forming energy storage; small signal stability; low-frequency oscillation

1 Introduction

The increased use of renewable energy has resulted in energy storage becoming an important method for mitigating renewable energy fluctuations and enhancing grid flexibility [1,2]. Currently, most existing energy storage systems are grid-following types that use phase-locked loops to track the voltage phase at the point of common coupling to achieve synchronization. However, phase-locked loops do not perform well in weak grids and cannot accurately track the voltage phase at the point of common coupling (PCC), which means that grid-following energy storage systems are unable to operate normally [3]. However, the continuous integration of renewable energy can lead to reduced grid strength, which means that grid-following energy storage will face adaptation difficulties in the future.

Grid-forming energy storage does not use phase-locked loops. Instead, it employs a power synchronization control strategy similar to generators and achieves synchronization through its own power deviation. In contrast to grid-following energy storage, grid-forming energy storage can autonomously establish grid voltage, has voltage source characteristics, provides inertia support and damping to the system, and can better adapt to the "double-high" characteristics of substantial renewable energy and power electronics penetration [4,5].

Previous research on grid-forming energy storage primarily focused on utilizing the inherent energy storage functions associated with peak shaving and frequency regulation. However, the grid-forming energy storage characteristics strongly depend on electronic power converters and their control strategies. In recent years, wide-band oscillations caused by interactions between electronic power converter control loops and the grid have frequently occurred and these have seriously affected the stable operation of power systems [6–8]. Therefore, the small-signal stability issues associated with grid-forming energy storage cannot be ignored. For example, Reference [9] establishes a unified modular small-signal model for grid-forming inverters and verifies its effectiveness through eigenvalue analysis and time-domain simulations. However, it fails to elucidate the dynamic mechanisms behind key eigenvalue trajectories and their impacts on system performance. Reference [10] constructed a state-space model for grid-forming energy storage for an offshore wind farm and used a sensitivity analysis to obtain the impacts of key parameters and grid strength on system dynamic behavior. Reference [11] establishes small-signal models for parallel grid-forming converters ranging from single-unit to multi-unit systems and provides mathematical stability analysis. However, it does not delve into clarifying the key physical mechanisms that influence system stability. These studies all used the system state-space model and sensitivity and eigenvalue analysis methods to analyze the small-signal stability of the system. This approach is theoretically rigorous and accurate, but computationally intensive, complex to solve, and difficult to scale up. Reference [12] clarifies the equivalent impedance of voltage and current loops by establishing a sequence impedance model for grid-forming converters and verifies the advantages of the single-power-loop structure. However, its explanation of the dynamic interaction mechanisms between control loops remains insufficiently in-depth. Reference [13] proposes a modular three-port admittance modeling framework that effectively addresses the challenge of impedance modeling in hybrid AC/DC systems containing grid-following and grid-forming converters, demonstrating good universality. However, its analysis of the internal interactions within the system and the intrinsic stability mechanisms remains insufficient. Similarly, Reference [14] established impedance matrix models for grid-forming converters in a synchronous rotating coordinate system and a coordinate system defined by the dynamic angular frequency of the power system. These studies concluded that the two impedance modeling methods were equivalent, but the latter better explained system behavior during disturbances. Furthermore, each study analyzed the small-signal stability of the system by establishing frequency-domain impedance models. Overall, the proposed models have strong scalability but increase the complexity of the stability analysis. However, the physical meaning of coupled impedance remains unclear.

Compared to eigenvalue and impedance analysis methods, the damping torque analysis method has clear physical meaning and can effectively separate and quantify the coupling effects of multiple factors. Reference [15] constructed a multi-loop damping path model of a virtual synchronous generator control system based on the embedded torque method. The results showed that there were interactive influences between the d-axis and q-axis components of the voltage control loop and current control loop of the virtual synchronous generator. The malignant competition and negative incentive of the damping torque between these interactive loops meant that the oscillation modes were unstable. However, the entire damping loop was overly complex and difficult to analyze. Reference [16] established a damping path model for a wind farm and grid-forming energy storage and concluded that grid-forming energy storage can provide certain levels of damping that can suppress wide-band oscillations caused by wind farms connected to weak grids. Reference [17], establishing a single-input single-output dynamic interaction model, reveals the excellent dynamic characteristics of grid-forming energy storage in weak grids and its impact on grid-following photovoltaics. However, due to the inherent limitations of the single-input single-output model, it is difficult to fully uncover the complex dynamic coupling relationships between the multiple control loops within these systems. In summary, the damping torque analysis method has clear physical meaning and can effectively achieve the separation and quantitative assessment of multi-factor coupling effects. However, previous studies treated the research system as a whole when conducting damping torque analyses and analyzed the damping characteristics of the entire system without examining internal interactions.

Based on this analysis of previous studies, the novel contributions made by this study are as follows:

(1) Constructed a multi-timescale model of a grid-forming energy storage grid-connected system. Derived a full-order mathematical model for the grid-forming energy storage system and used a participation factor analysis to establish a reduced-order model and a multi-damping torque model, which provided a theoretical foundation that explained the internal dynamic interaction mechanisms associated with the system.

(2) Quantitative evaluation of the system damping characteristics from a damping perspective. A constructed multi-damping torque model was used to systematically and quantitatively evaluate the impact of grid strength, operating conditions, and control parameters on the low-frequency oscillation damping characteristics of the grid-forming energy storage system from a damping perspective.

(3) Comprehensive validation through theoretical analysis and time-domain simulation. The theoretical analysis results were fully verified using time-domain simulation methods. The results confirmed the accuracy and effectiveness of the proposed model and analysis approach. This showed that the conclusions were reliable and had strong engineering applicability. They also provide theoretical guidance for tuning the control parameters in grid-forming energy storage systems.

2 Mathematical Model of a Grid-Forming Energy Storage Grid-Connected System

2.1 Grid-Forming Energy Storage Grid-Connected System

The isolation effect of the DC/AC converter and the large support capacitor on the DC side meant that this study equivalently modeled the DC/DC module as an ideal DC voltage source and did not consider the dynamic process on the DC side when establishing a small-signal model of a grid-forming energy storage grid-connected system. The model for the grid-forming energy storage grid-connected system is shown in Fig. 1.

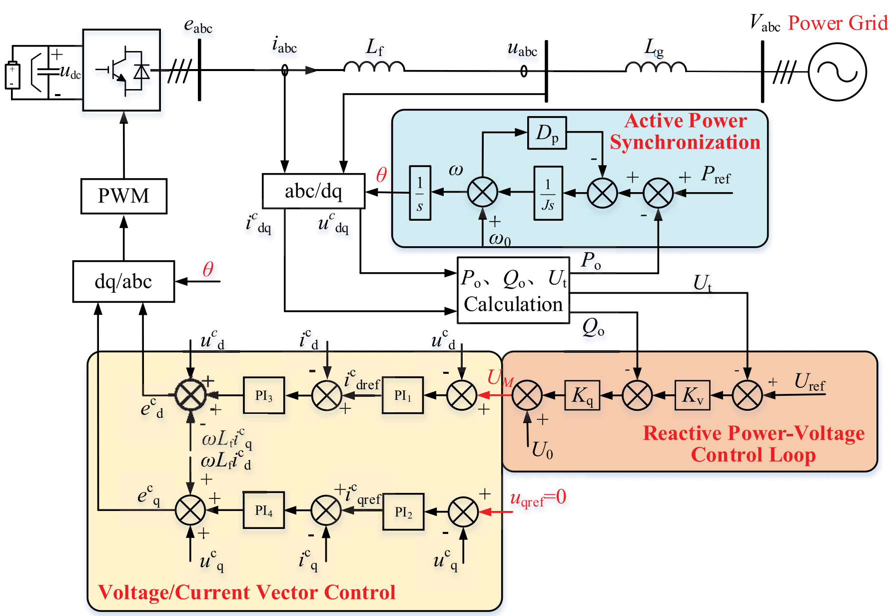

Figure 1: Grid-forming energy storage grid-connected system model

Where u_{dc} represents the DC voltage; e_{abc} represents the three-phase output voltage of the grid-forming energy storage system; i_{abc} represents the three-phase output current of the grid-forming energy storage system; u_{abc} represents the three-phase voltage at the PCC of the grid-forming energy storage system; V_{abc} represents the three-phase grid voltage; and L_f and L_g represent filter inductance and line inductance, respectively.

2.2 Mathematical Model of the Grid-Forming Energy Storage Grid-Connected System

The mathematical model for the system shown in Fig. 1 contains five parts: grid-forming energy storage filter inductance, active power synchronization, a reactive power-voltage control loop, voltage/current vector control, and an AC grid. The dynamic equation for filter inductance is shown in Eq. (1):

$$\begin{cases} L_f \dfrac{di_d}{dt} = e_d - u_d + \omega_0 L_f i_q \\ L_f \dfrac{di_q}{dt} = e_q - u_q - \omega_0 L_f i_d \end{cases}, \tag{1}$$

where L_f represents the filter inductance; i_d and i_q represent the d-axis and q-axis components of the output current of the grid-forming converter in the main circuit coordinate system, respectively; e_d and e_q represent the d-axis and q-axis components of the output voltage of the grid-forming energy storage system in the main circuit coordinate system, respectively; and u_d and u_q represent the d-axis and q-axis components of the voltage at the PCC of the grid-forming energy storage system in the main circuit coordinate system, respectively.

Active power synchronization is used to achieve self-synchronization in grid-forming energy storage systems. Its output phase is used for the park and inverse transformations of three-phase signals to realize vector control of grid-forming energy storage. Its dynamic equation is shown in Eq. (2):

$$\begin{cases} J \dfrac{d\omega}{dt} = P_{ref} - P_o - D_p(\omega - \omega_0) \\ \dfrac{d\theta}{dt} = \omega \end{cases}, \tag{2}$$

where J represents the virtual moment of inertia; ω represents the virtual angular acceleration; P_{ref} represents the reference power of the grid-forming converter; D_p represents the virtual damping coefficient; ω_0 represents the virtual reference angular acceleration; θ represents the virtual phase angle; and P_o represents the output active power of the grid-forming energy storage system, with its expression given as follows:

$$P_o = 1.5 u_d i_d + 1.5 u_q i_q. \tag{3}$$

The reactive power-voltage control loop is used to generate the d-axis voltage reference value at the PCC to achieve voltage vector orientation. Its dynamic equation is shown in Eq. (4):

$$U_M = ((U_{ref} - U_t) K_v - Q_o) K_q + U_0, \tag{4}$$

where K_v represents the voltage droop coefficient; K_q represents the reactive power-voltage regulation coefficient; U_0 represents the reference voltage; U_M represents the d-axis voltage reference value at the PCC generated by the reactive power-voltage control loop; U_{ref} represents the reference value of the phase voltage amplitude; U_{t} represents the phase voltage amplitude; and Q_{o} represents the output reactive power of the grid-forming energy storage system, which is calculated as follows:

$$\begin{cases} U_{\mathrm{t}} = \sqrt{u_{\mathrm{d}}^{2} + u_{\mathrm{q}}^{2}} \\ Q_{\mathrm{o}} = 1.5u_{\mathrm{q}}i_{\mathrm{d}} - 1.5u_{\mathrm{d}}i_{\mathrm{q}} \end{cases}. \tag{5}$$

The grid-forming energy storage system has a voltage d-axis orientation. Based on the output voltage from the reactive power-voltage control loop, the active current reference value $i^{c}{}_{\mathrm{dref}}$ and the reactive current reference value $i^{c}{}_{\mathrm{qref}}$ in the control coordinate system are dynamically generated through the voltage outer loop control. The mathematical model is as follows:

$$\begin{cases} i^{\mathrm{c}}{}_{\mathrm{dref}} = \left(U_{\mathrm{M}} - u^{\mathrm{c}}{}_{\mathrm{d}}\right)\left(k_{\mathrm{p1}} + \dfrac{k_{\mathrm{i1}}}{s}\right) \\ i^{\mathrm{c}}{}_{\mathrm{qref}} = \left(u_{\mathrm{qref}} - u^{\mathrm{c}}{}_{\mathrm{q}}\right)\left(k_{\mathrm{p2}} + \dfrac{k_{\mathrm{i2}}}{s}\right) \end{cases}, \tag{6}$$

where $u^{c}{}_{\mathrm{d}}$ and $u^{c}{}_{\mathrm{q}}$ represent the d-axis and q-axis components of the voltage at the PCC of the grid-forming energy storage system in the control coordinate system, respectively; k_{p1} and k_{i1} represent the proportional and integral coefficients of the active voltage outer loop, respectively; and k_{p2} and k_{i2} represent the proportional and integral coefficients of the reactive voltage outer loop, respectively. The q-axis voltage reference value u_{qref} at the PCC was set to 0.

The current inner loop control, based on the voltage constraint equation, regulates the output voltage of the grid-forming energy storage system to ensure the active/reactive currents track their reference values. The mathematical model for the d-axis and q-axis components ($e^{c}{}_{\mathrm{d}}$ and $e^{c}{}_{\mathrm{q}}$) of the grid-forming energy storage system output voltage in the control coordinate system is as follows:

$$\begin{cases} e^{\mathrm{c}}{}_{\mathrm{d}} = \left(i^{\mathrm{c}}{}_{\mathrm{dref}} - i^{\mathrm{c}}{}_{\mathrm{d}}\right)\left(k_{\mathrm{p3}} + \dfrac{k_{\mathrm{i3}}}{s}\right) - \omega L_{\mathrm{f}} i^{\mathrm{c}}{}_{\mathrm{q}} + u^{\mathrm{c}}{}_{\mathrm{d}} \\ e^{\mathrm{c}}{}_{\mathrm{q}} = \left(i^{\mathrm{c}}{}_{\mathrm{qref}} - i^{\mathrm{c}}{}_{\mathrm{q}}\right)\left(k_{\mathrm{p4}} + \dfrac{k_{\mathrm{i4}}}{s}\right) + \omega L_{\mathrm{f}} i^{\mathrm{c}}{}_{\mathrm{d}} + u^{\mathrm{c}}{}_{\mathrm{q}} \end{cases}, \tag{7}$$

where $i^{c}{}_{\mathrm{d}}$ and $i^{c}{}_{\mathrm{q}}$ represent the d-axis and q-axis components of the output current of the grid-forming energy storage system in the control coordinate system, respectively; k_{p3} and k_{i3} represent the proportional and integral coefficients of the active current inner loop, respectively; and k_{p4} and k_{i4} represent the proportional and integral coefficients of the reactive current inner loop, respectively.

The mapping relationship between the voltage and current d/q-axis components in the control coordinate system and the voltage and current d/q-axis components in the main circuit coordinate system is as follows:

$$\begin{cases} u^{\mathrm{c}}{}_{\mathrm{d}} = u_{\mathrm{d}} + u_{\mathrm{q0}}\theta \\ u^{\mathrm{c}}{}_{\mathrm{q}} = u_{\mathrm{q}} - u_{\mathrm{d0}}\theta \end{cases}, \begin{cases} i^{\mathrm{c}}{}_{\mathrm{d}} = i_{\mathrm{d}} + i_{\mathrm{q0}}\theta \\ i^{\mathrm{c}}{}_{\mathrm{q}} = i_{\mathrm{q}} - i_{\mathrm{d0}}\theta \end{cases}, \tag{8}$$

where u_{d0} and u_{q0} represent the d-axis and q-axis components of the initial voltage value at the PCC of the grid-forming energy storage system, respectively, and i_{d0} and i_{q0} represent the d-axis and q-axis components of the initial output current value for the grid-forming energy storage system, respectively.

The dynamic model of the AC grid line inductance is represented by the following equation:

$$\begin{cases} L_g \dfrac{\mathrm{d}i_d}{\mathrm{d}t} = u_d - V_d + \omega_0 L_g i_q \\ L_g \dfrac{\mathrm{d}i_q}{\mathrm{d}t} = u_q - V_q - \omega_0 L_g i_d \end{cases}, \tag{9}$$

where V_d and V_q represent the d-axis and q-axis components of the grid voltage in the main circuit coordinate system, respectively.

Eqs. (1)–(9) constitute the mathematical model for the grid-forming energy storage grid-connected system. The linearized state-space model at the equilibrium point is as follows:

$$\Delta\dot{X} = A\Delta X + B\Delta U, \tag{10}$$

where $\Delta X = [\Delta i_d, \Delta i_q, \Delta x_1, \Delta x_2, \Delta x_3, \Delta x_4, \Delta\omega, \Delta\theta]$ represents the small-signal form of the state variables. The state variables Δi_d and Δi_q denote the small-signal disturbance components of the active current and reactive current, respectively; Δx_1–Δx_4 are defined as intermediate state variables in the control system, corresponding to the dynamic processes of the active power-voltage outer loop, reactive power-voltage outer loop, active current inner loop, and reactive current inner loop; $\Delta\omega$ represents the small-signal disturbance component of the virtual angular velocity, and $\Delta\theta$ represents the small-signal disturbance component of the virtual phase angle. $\boldsymbol{A}$ and $\boldsymbol{B}$ denote the state matrix and input matrix of the system, respectively, where the positive real part eigenvalues of the state matrix A reflect the oscillatory instability modes of the system, and the risk of instability increases as the real part of the eigenvalues shifts toward the positive direction of the real axis. The detailed expression of the state matrix $\boldsymbol{A}$ is provided in Appendix A.

3 Grid-Forming Energy Storage Multi-Damping Path Model

3.1 Multi-Timescale Decomposition Analysis of the Model

To simplify the subsequent analysis, the linearized state-space model of the grid-forming energy storage grid-connected system obtained in Section 2.2 was reduced in order. The eigenvalues of the system when the grid strength is 7.2 and P_o = 0.5 MW are listed in Table 1.

Table 1: Full-order system eigenvalues

Mode	Eigenvalue	Oscillation frequency/Hz
λ_1	−34.9	/
λ_2	−3.2	/
$\lambda_{3/4}$	$-0.08 \pm j21.5$	3.4
$\lambda_{5/6}$	$-2247.6 \pm j76.4$	12.2
$\lambda_{7/8}$	$-380.9 \pm j1.4$	0.2

The system contains one subsynchronous oscillation mode $\lambda_{5/6}$ (12.2 Hz) and two low-frequency oscillation modes $\lambda_{3/4}$ (3.4 Hz) and $\lambda_{7/8}$ (0.2 Hz). The eigenvalue for $\lambda_{3/4}$ dominates the low-frequency oscillation mode of the system.

The participation factors associated with the eigenvalue for $\lambda_{3/4}$ are shown in Fig. 2. The dominant low-frequency oscillation eigenvalue for $\lambda_{3/4}$ is primarily influenced by the active voltage outer loop and reactive voltage outer loop control stages. The power synchronization stage has a minimal effect and the current inner loop control has almost no influence. Furthermore, when the bandwidth of the current inner loop is significantly higher than that of the voltage outer loop, the dynamic behavior of the current inner loop can be largely ignored, which means that the current rapidly tracks its reference value and achieves quasi-steady-state control.

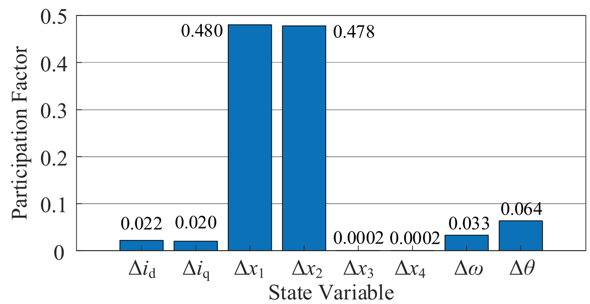

Figure 2: Participating factors associated with the dominant eigenvalue for $\lambda_{3/4}$

Based on the above analysis, the updated reduced-order state-space model that ignores the dynamics of the current inner loop is as follows:

$$\Delta\dot{X}_1 = A_1\Delta X_1 + B_1\Delta U_1, \tag{11}$$

where $\Delta X_1 = [\Delta x_1, \Delta x_2, \Delta\omega, \Delta\theta]$ and $\boldsymbol{A}_1$ and $\boldsymbol{B}_1$ represent the state and input matrices of the system, respectively. The detailed expression of the state matrix $\boldsymbol{A}_1$ is provided in Appendix B. The eigenvalues of the reduced-order model under a grid strength of 7.2 and P_o = 0.5 MW are shown in Table 2. The eigenvalue for $\lambda_{3/4}$ dominates the low-frequency oscillation mode of the system with an oscillation frequency of 3.58 Hz. The deviation from the oscillation frequency produced by the detailed model (3.4 Hz) is 0.18 Hz, which falls within an acceptable range and confirms the accuracy and effectiveness of the reduced-order model.

Table 2: Reduced-order system eigenvalues

Mode	Eigenvalue	Oscillation frequency/Hz
λ_1	−34.8	/
λ_2	−3.2	/
$\lambda_{3/4}$	$-0.08 \pm j22.5$	3.58

3.2 Multi-Damping Path Model

A single-input single-output transfer function block diagram of the grid-forming energy storage system was established based on the reduced-order model of the system, as shown in Fig. 3:
where $G_1 = k_{p1} + k_{i1}/s$ represents the active voltage outer loop control link and $G_2 = k_{p2} + k_{i2}/s$ represents the reactive voltage outer loop control link.

The output active power can be expressed using system-related state variables. The detailed derivation process is provided in Appendix C. The expression for output active power is as follows:

$$\Delta P_o = D_p\Delta\omega + \left(K_1 + \frac{K_2}{s}\right)\Delta\theta + \frac{K_3}{s}\Delta u_d + \frac{K_4}{s}\Delta u_q + \frac{K_5}{s}\Delta i_q, \tag{12}$$

where K_1–K_5 represent the power amplification coefficients, and their specific expressions are detailed in Eq. (A21) of Appendix C.

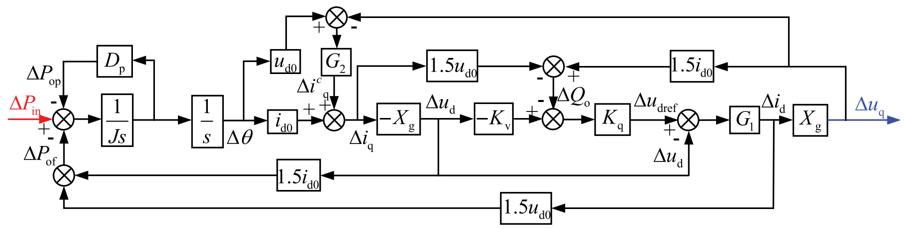

Figure 3: Block diagram of the single input and single output transfer functions for grid-forming energy storage

The expressions for Δu_d, Δu_q, Δi_q, and $\Delta\theta$ are given by the following equations:

$$\begin{cases} \Delta u_d = G_{ud}(s)\,\Delta\theta \\ \Delta u_q = G_{uq}(s)\,\Delta\theta \\ \Delta i_q = G_{iq}(s)\,\Delta\theta \\ \Delta\theta = \dfrac{1}{s}\Delta\omega \end{cases}, \tag{13}$$

where $G_{ud}(s)$ represents the transfer function from $\Delta\theta$ to Δu_d; $G_{uq}(s)$ represents the transfer function from $\Delta\theta$ to Δu_q; and $G_{iq}(s)$ represents the transfer function from $\Delta\theta$ to Δi_q. The specific expressions for $G_{ud}(s)$, $G_{uq}(s)$, and $G_{iq}(s)$ are detailed in Eqs. (A15) and (A17) of Appendix C.

Fig. 4 shows a single-input single-output model of the grid-forming energy storage system that is based on the above analyses. This model incorporates five power feedback loops.

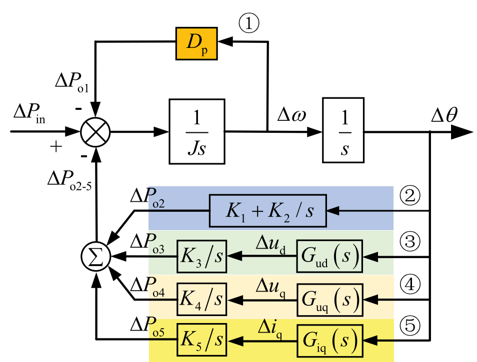

Figure 4: Single input single output model of grid-forming energy storage

Reference [18] first applied the damping torque analysis method to analyze the impact of excitation control systems on low-frequency oscillations in synchronous machines. The torque generated by excitation changes can be divided into two components: the synchronizing torque $\Delta M_S\Delta\delta$, which is proportional to $\Delta\delta$, and the damping torque $\Delta M_D\Delta\delta$, which is proportional to the rotational speed $s\Delta\delta$. A block diagram of the second-order equivalent model for the synchronous machine is shown in Fig. 5.

Fig. 5 shows that the virtual rotor dynamics of the grid-forming energy storage grid-connected system. $\Delta P_{in} - \Delta P_o = Js\Delta\omega$ has a structure that is similar to the rotor dynamics of a synchronous machine: $\Delta M_m - \Delta M_e = T_J s\Delta\omega$. Based on this similarity, the damping torque method was adopted to analyze the low-frequency oscillation characteristics of the grid-forming energy storage grid-connected system. The relationship between the virtual angular acceleration $\Delta\omega$ and the output power ΔP_o is as follows:

$$\Delta P_{oi} = \Phi_i(s)\,\Delta\omega, \tag{14}$$

where the expressions for $\Phi_i(s)$ (I = 1, 2, 3, 4, 5) are as follows:

$$\begin{cases} \Phi_1(s) = D_{\mathrm{p}} \\ \Phi_2(s) = \dfrac{1}{s}\left(K_1 + \dfrac{K_2}{s}\right) \\ \Phi_3(s) = \dfrac{1}{s}\left(G_{\mathrm{ud}}(s)\,\dfrac{K_3}{s}\right) \\ \Phi_4(s) = \dfrac{1}{s}\left(G_{\mathrm{uq}}(s)\,\dfrac{K_4}{s}\right) \\ \Phi_5(s) = \dfrac{1}{s}\left(G_{\mathrm{iq}}(s)\,\dfrac{K_5}{s}\right) \end{cases}. \tag{15}$$

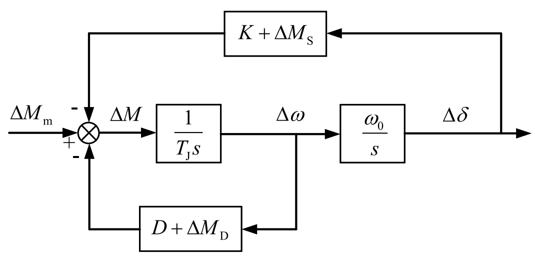

Figure 5: Block diagram of a second-order equivalent model for a synchronous machine

When a low-frequency oscillation disturbance occurs, all the state variables associated with the system oscillate at the same frequency ω_s. Therefore, by substituting $s = j\omega_s$ into the power feedback transfer function, the power feedback transfer function can be expressed in the following form:

$$\frac{\Delta P_{oi}}{\Delta\omega} = \mathrm{Re}\left[\Phi_i(j\omega_s)\right] + j\,\mathrm{Im}\left[\Phi_i(j\omega_s)\right]. \tag{16}$$

According to Eq. (16) and $s = j\omega_s$, Eq. (14) can be transformed into the following form:

$$\Delta P_{oi} = \mathrm{Re}\left[\Phi_i(j\omega_s)\right]\Delta\omega + \frac{-\mathrm{Im}\left[\Phi_i(j\omega_s)\right]\omega_s}{s}\Delta\omega. \tag{17}$$

Therefore, the power feedback loop of the system can be decomposed into the following form:

$$\Delta P_{oi} = \left(D_i(\omega_s) + \frac{K_i(\omega_s)}{s}\right)\Delta\omega. \tag{18}$$

A multi-damping path model for the grid-forming energy storage grid-connected system can then be obtained, as shown in Fig. 6.

$D_i(\omega_s)$ is the equivalent damping coefficient for each branch and $K_i(\omega_s)$ is the equivalent synchronizing coefficient for each branch. The expressions for $D_i(\omega_s)$ and $K_i(\omega_s)$ are given by the following equations:

$$\begin{cases} D_1(j\omega_s) = D_{\mathrm{p}} \\ D_2(j\omega_s) = \mathrm{Re}\left(\dfrac{1}{j\omega_s}\left(K_1 + \dfrac{K_2}{j\omega_s}\right)\right) \\ D_3(j\omega_s) = \mathrm{Re}\left(\dfrac{1}{j\omega_s}\left(G_{ud}(j\omega_s)\dfrac{K_3}{j\omega_s}\right)\right) \\ D_4(j\omega_s) = \mathrm{Re}\left(\dfrac{1}{j\omega_s}\left(G_{uq}(j\omega_s)\dfrac{K_4}{j\omega_s}\right)\right) \\ D_5(j\omega_s) = \mathrm{Re}\left(\dfrac{1}{j\omega_s}\left(G_{iq}(j\omega_s)\dfrac{K_5}{j\omega_s}\right)\right) \end{cases}, \begin{cases} K_1(j\omega_s) = 0 \\ K_2(j\omega_s) = -\mathrm{Im}\left(\dfrac{1}{j\omega_s}\left(K_1 + \dfrac{K_2}{j\omega_s}\right)\right)\omega_s \\ K_3(j\omega_s) = -\mathrm{Im}\left(\dfrac{1}{j\omega_s}\left(G_{ud}(j\omega_s)\dfrac{K_3}{j\omega_s}\right)\right)\omega_s \\ K_4(j\omega_s) = -\mathrm{Im}\left(\dfrac{1}{j\omega_s}\left(G_{uq}(j\omega_s)\dfrac{K_4}{j\omega_s}\right)\right)\omega_s \\ K_5(j\omega_s) = -\mathrm{Im}\left(\dfrac{1}{j\omega_s}\left(G_{iq}(j\omega_s)\dfrac{K_5}{j\omega_s}\right)\right)\omega_s \end{cases}. \tag{19}$$

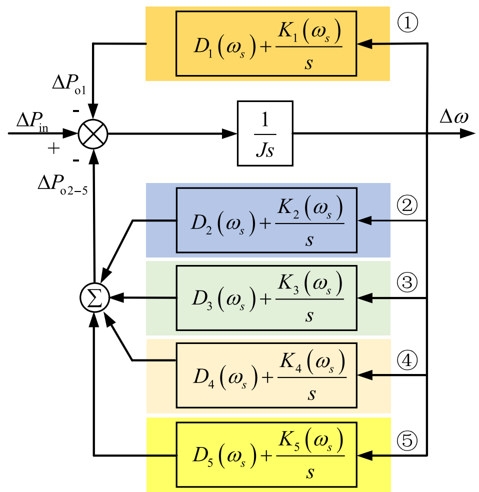

Figure 6: Grid-forming energy storage multi-damping path model

3.3 Stability Criterion

Based on the grid-forming energy storage multi-damping-path model, this section derives the system stability indicators. To simplify the analysis, the multi-damping-path model of the grid-forming energy storage is equivalently represented as a second-order model using the superposition principle of transfer functions, as shown in Fig. 7.

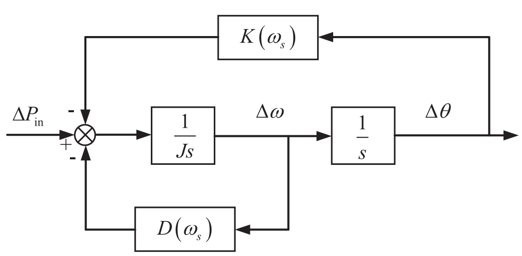

Figure 7: Block diagram of the second order equivalent model for grid-forming energy storage

$D(\omega_s)$ and $K(\omega_s)$ are the damping coefficient and synchronizing coefficient, respectively. Their specific expressions are given by the following equations:

$$\begin{cases} D(\omega_s) = D_1(\omega_s) + D_2(\omega_s) + D_3(\omega_s) + D_4(\omega_s) + D_5(\omega_s) \\ K(\omega_s) = K_1(\omega_s) + K_2(\omega_s) + K_3(\omega_s) + K_4(\omega_s) + K_5(\omega_s) \end{cases}. \tag{20}$$

Fig. 7 shows that the closed-loop transfer function of the system is as follows:

$$\frac{\Delta\theta}{\Delta P_{in}} = \frac{1}{Js^2 + D\left(\omega_s\right)s + K\left(\omega_s\right)}, \tag{21}$$

and the characteristic roots of Eq. (21) are

$$s_{1,2} = -\frac{D\left(\omega_s\right)}{2J} \pm \frac{1}{2}\sqrt{\left(\frac{D\left(\omega_s\right)}{J}\right)^2 - 4\frac{K\left(\omega_s\right)}{J}}. \tag{22}$$

Based on the analysis of the characteristic roots (Eq. (22)), the stability criteria can be summarized as follows:

(1) When $K(\omega_s) < 0$, the equation has a positive real root and the system experiences a runaway loss of synchronization.

(2) When $K(\omega_s) > 0$ and $D(\omega_s) < 0$, the equation has a pair of conjugate complex roots with a positive real part and the system experiences oscillatory instability.

(3) When $K(\omega_s) > 0$ and $D(\omega_s) > 0$, the system remains stable.

4 Grid-Forming Energy Storage Low-Frequency Oscillation Analysis

In this section, a quantitative evaluation is conducted to assess the impact of control parameters, operating conditions, and grid strength on the low-frequency oscillation characteristics of grid-forming energy storage systems. The influence patterns of key control parameters on system low-frequency oscillations are systematically elucidated. Based on the grid-forming energy storage grid-connected system model shown in Fig. 1, an electromagnetic transient simulation model is built in the PSCAD/EMTDC platform to verify the correctness of the aforementioned damping model analysis conclusions. The key parameters of the model are listed in Table 3.

Table 3: System parameters

Symbol	System parameters	Values/Unit
P	Rated power	1.5/kV
u_{dc}	DC bus voltage	1.2/F
C	DC bus capacitance	0.09/H
L_{f}	Filter inductance	0.0001/H
L_{g}	Grid line inductance	0.00014/kV
/	Grid rated voltage	0.69/kV
J	Virtual inertia	0.1
D_{p}	Virtual damping	3.56
K_{v}	Voltage droop coefficient	1
K_{q}	Reactive voltage regulation coefficient	0.1
$k_{\mathrm{p1}}/k_{\mathrm{i1}}$	Active voltage proportional/integral	0.5/300
$k_{\mathrm{p2}}/k_{\mathrm{i2}}$	Reactive voltage proportional/integral	0.5/300
$k_{\mathrm{p3}}, k_{\mathrm{i3}}$	Active current proportional/integral	0.3/100
$k_{\mathrm{p4}}, k_{\mathrm{i4}}$	Reactive current proportional/integral	0.3/100

4.1 Analysis of the Damping Characteristics under Different Grid Strength Conditions

The quantitative analysis results for the five Damping Paths constructed for the grid-forming energy storage grid-connected system when the Short-Circuit Ratio (SCR) ranged from 7.2 to 8.4 are shown in Fig. 8 and Table 4. Damping Paths 3 and 5 dominated the total damping of the system and primarily provided negative damping. As the grid strength increased, the negative damping intensified, which degraded system stability. Furthermore, Damping Paths 3 and 5 were strongly correlated with the active voltage Δu_d, and changes in Δu_d strongly influenced the active power output of the system. When the grid strength was less than 7.9, Damping Paths 3 and 5 introduced negative damping, but the inherent virtual damping (Damping Path 1) compensated for the negative damping introduced as the grid strength increased. When the grid strength exceeded 7.82, the inherent virtual damping could not counteract the negative damping contributed by Damping Paths 3 and 5, which led to negative total damping and system instability.

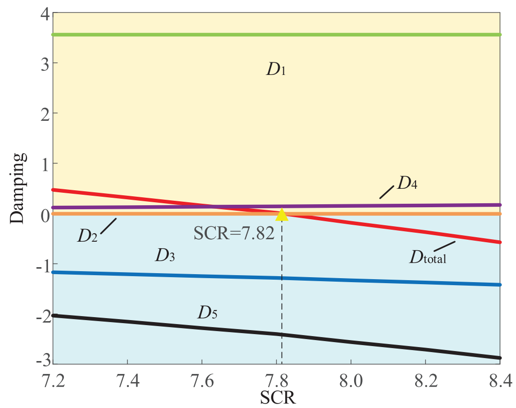

Figure 8: Characteristic damping curves under different power grid intensities

Table 4: Damping under different power grid intensities

SCR	D_1	D_2	D_3	D_4	D_5	D_{total}
7.6	3.56	−0.0061	−1.2477	0.1344	−2.2814	0.1592
7.8	3.56	−0.0064	−1.2824	0.1421	−2.3990	0.0143
8.0	3.56	−0.0069	−1.3302	0.1515	−2.5602	−0.1858

The response curves for the active power P_o and reactive power Q_o of the system under the different grid strengths at t = 15 s when the grid strength was 5.1 to 7.6 (blue curve) and 8.0 (red curve) are shown in Fig. 9. When the grid strength was 8.0, the P_o and Q_o of the system showed low-frequency oscillatory instability with an oscillation frequency of 3.4 Hz. However, when the grid strength was 7.6, P_o and Q_o showed damped oscillations and the system was stable. The simulation results were consistent with the theoretical analysis and showed that grid-forming energy storage is prone to low-frequency oscillations under strong grid conditions.

4.2 Analysis of the Damping Characteristics under Different Operating Conditions

The quantitative analysis results for the five damping paths constructed for the grid-forming energy storage grid-connected system when the operating condition ranged from 0.1 to 1.3 MW are shown in Fig. 10 and Table 5. Damping Paths 3 and 5 dominated the total damping of the system and primarily provided negative damping. As the operating power decreased, the negative damping increased, which degraded system stability. Damping Paths 3 and 5 were highly correlated with the active voltage (Δu_d) and changes in Δu_d strongly influenced the active power output of the system. When the operating power exceeded 0.51 MW, Damping Paths 3 and 5 provided negative damping, but the inherent virtual damping (Damping Path 1) compensated for the negative damping introduced as the operating power decreased. However, when the operating power fell below 0.51 MW, Damping Path 1 could not counteract the negative damping due to Damping Paths 3 and 5, resulting in negative total damping and system instability.

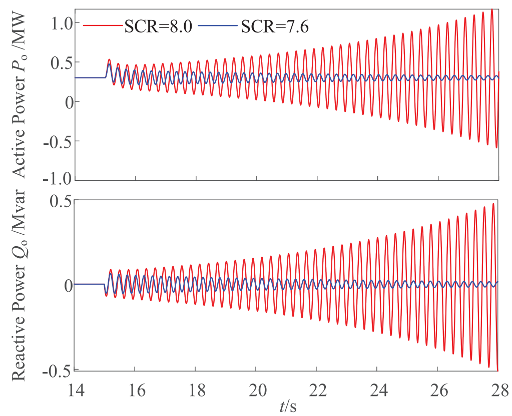

Figure 9: P_o and Q_o response curves under different power grid intensities

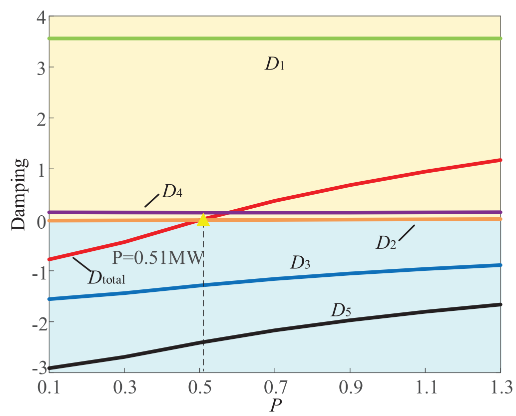

Figure 10: Characteristic damping curves under different working conditions

Table 5: Damping under different working conditions

P	D_1	D_2	D_3	D_4	D_5	D_{total}
0.5	3.56	−0.0065	−1.2891	0.1414	−2.4117	−0.0059
0.7	3.56	−0.0011	−1.1591	0.1421	−2.1684	0.3727
0.9	3.56	0.0043	−1.0536	0.1418	−1.9711	0.6814

The response curves for the active power increment (ΔP_o) and reactive power increment (ΔQ_o) of the system under different operating conditions at t = 15 s and when the grid strength ranged from 5.1 to 7.8 are shown in Fig. 11. The blue curve represents P_o = 1.3 MW and the red curve represents P_o = 0.1 MW. When P_o = 0.1 MW, the active power P_o and reactive power Q_o of the system showed low-frequency oscillatory instability with an oscillation frequency of 3.3 Hz. However, when P_o = 1.3 MW, P_o and Q_o showed damped oscillations and the system was stable. The simulation results were consistent with the theoretical analysis and showed that grid-forming energy storage is prone to low-frequency oscillations under low operating conditions.

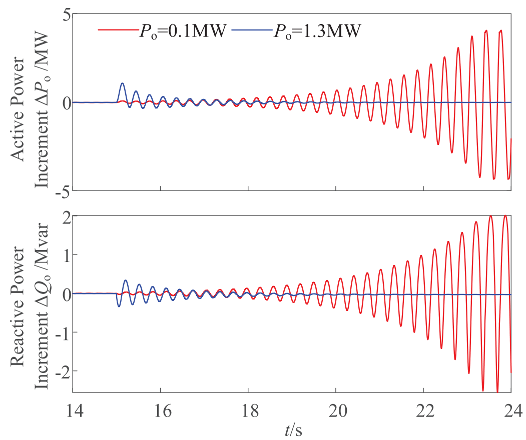

Figure 11: ΔP_o and ΔQ_o response curves under different working conditions

4.3 Analysis of the Damping Characteristics under Different Reactive Power-Voltage Regulation Coefficients (K_q)

The quantitative analysis results for the five damping paths when the reactive power-voltage regulation coefficient K_q ranged from 0.07 to 0.13, are shown in Fig. 12 and Table 6. Damping Paths 3 and 5 dominated the total damping of the system and primarily provided negative damping. As K_q decreased, the negative damping intensified, which degraded system stability. Damping Paths 3 and 5 were highly correlated with the active voltage Δu_d, and changes in Δu_d strongly influenced the active power output of the system. When K_q exceeded 0.099, Damping Paths 3 and 5 led to negative damping; however the inherent virtual damping (Damping Path 1) compensated for the negative damping introduced as K_q decreased. When K_q fell below 0.099, Damping Path 1 could not counteract the negative damping contributed by Damping Paths 3 and 5, which led to negative total damping and system instability.

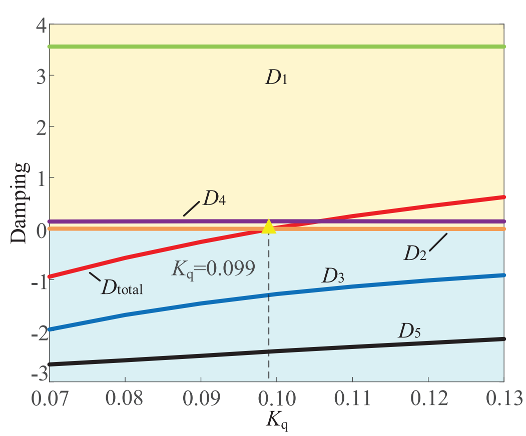

Figure 12: Damping characteristic curves at different K_q levels

Table 6: Damping at different K_q values

K_q	D_1	D_2	D_3	D_4	D_5	D_{total}
0.09	3.56	−0.0054	−1.4662	0.1412	−2.4912	−0.2616
0.10	3.56	−0.0064	−1.2824	0.1421	−2.3990	0.0143
0.11	3.56	−0.0073	−1.1360	0.1415	−2.3166	0.2416

The response curves for P_o and Q_o under different reactive power-voltage regulation coefficients (K_q) at t = 15 s when the grid strength increased from 5.1 to 7.8 are shown in Fig. 13. The blue curve represents K_q = 0.13, and the red curve represents K_q = 0.07. When K_q = 0.07, P_o and Q_o showed low-frequency oscillatory instability with an oscillation frequency of 3.1 Hz, but when K_q = 0.13, P_o and Q_o showed that the oscillations had been damped and the system was stable. The simulation results were consistent with the theoretical analysis and showed that appropriate increases in K_q within a certain range can enhance the stability of grid-forming energy storage systems.

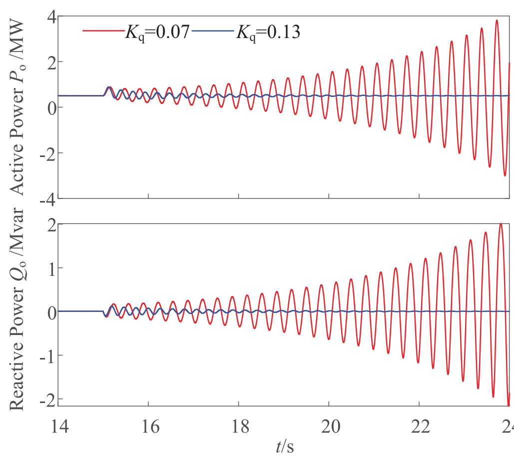

Figure 13: Response curves for P_o and Q_o at different K_q levels

4.4 Analysis of the Damping Characteristics under Different Active Voltage Outer Loop Proportional Coefficients (k_{p1})

The quantitative analysis results for the five damping paths when the active voltage outer loop proportional coefficient (k_{p1}) ranged from 0.07 to 0.13 are shown in Fig. 14 and Table 7. Damping Paths 3 and 5 dominated the total damping of the system and primarily provided negative damping. As k_{p1} decreased, the negative damping increased, which degraded system stability. Damping Paths 3 and 5 were highly correlated with Δu_d, and changes in Δu_d strongly influenced the active power output. When k_{p1} exceeded 0.48, Damping Paths 3 and 5 led to negative damping, but Damping Path 1 compensated for the negative damping that was introduced as k_{p1} decreased. However, when k_{p1} fell below 0.48, Damping Path 1 could not counteract the negative damping contributed by Damping Paths 3 and 5, resulting in negative total damping and system instability.

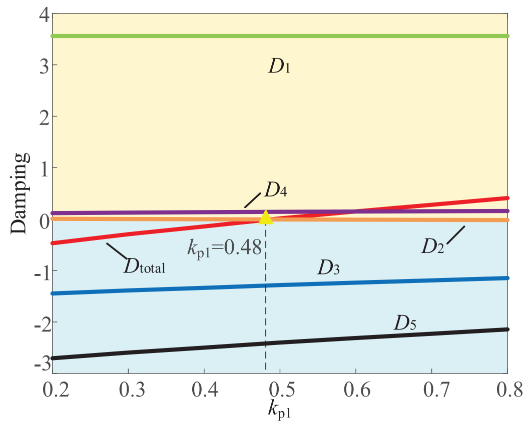

Figure 14: Characteristic damping curves at different k_{p1} levels

Table 7: Damping at different k_{p1} levels

k_{p1}	D_1	D_2	D_3	D_4	D_5	D_{total}
0.4	3.56	−0.0024	−1.3359	0.1346	−2.4991	−0.1428
0.5	3.56	−0.0064	−1.2824	0.1421	−2.3990	0.0143
0.6	3.56	−0.0104	−1.2357	0.1479	−2.3117	0.1501

The response curves for P_o and Q_o under different active voltage outer loop proportional coefficients (k_{p1}) at t = 15 s when the grid strength increased from 5.1 to 7.8 are shown in Fig. 15. The blue curve represents k_{p1} = 0.8 and the red curve represents k_{p1} = 0.2. When k_{p1} = 0.2, P_o and Q_o showed low-frequency oscillatory instability with an oscillation frequency of 3.4 Hz, but when k_{p1} = 0.8, P_o and Q_o showed that the oscillations had been damped and the system was stable. The simulation results were consistent with the theoretical analysis and showed that appropriate increases in k_{p1} within a certain range can enhance the stability of grid-forming energy storage systems.

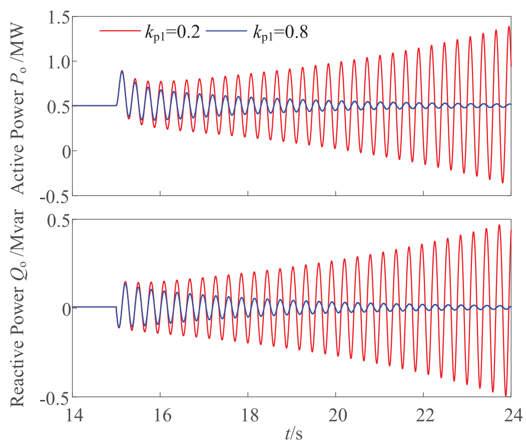

Figure 15: Response curves for P_o and Q_o at different k_{p1} levels

4.5 Analysis of the Damping Characteristics under Different Reactive Voltage Outer Loop Proportional Coefficients (k_{p2})

The quantitative analysis results for the five damping paths when the reactive voltage outer loop proportional coefficient (k_{p2}) ranged from 0.07 to 0.13 are shown in Fig. 16 and Table 8. Damping Paths 3 and 5 dominated the total damping of the system and primarily provided negative damping. As k_{p2} decreased, the negative damping intensified, which degraded system stability. Damping Paths 3 and 5 were highly correlated with Δu_d and changes in Δu_d strongly influenced the active power output. When k_{p2} exceeded 0.49, Damping Paths 3 and 5 led to negative damping, but Damping Path 1 compensated for the negative damping introduced as k_{p2} decreased. However, when k_{p2} fell below 0.49, Damping Path 1 could not counteract the negative damping contributed by Damping Paths 3 and 5, resulting in negative total damping and system instability.

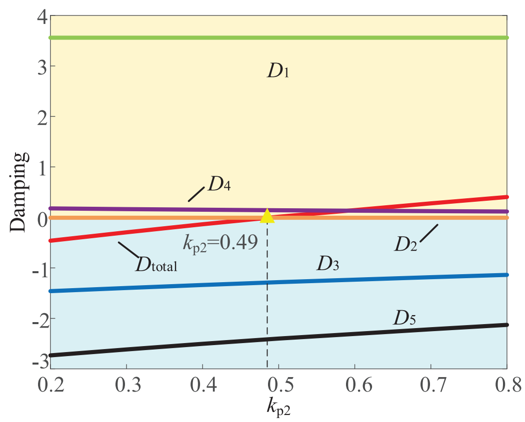

Figure 16: Characteristic damping curves at different k_{p2} levels

Table 8: Damping at different k_{p2} levels

k_{p2}	D_1	D_2	D_3	D_4	D_5	D_{total}
0.4	3.56	−0.0064	−1.3383	0.1525	−2.5036	−0.1358
0.5	3.56	−0.0064	−1.2824	0.1421	−2.3990	0.0143
0.6	3.56	−0.0064	−1.2336	0.1332	−2.3078	0.1454

The response curves for P_o and Q_o under different reactive voltage outer loop proportional coefficients (k_{p2}) at t = 15 s when the grid strength increased from 5.1 to 7.8 are shown in Fig. 17. The blue curve represents k_{p2} = 0.8, and the red curve represents k_{p2} = 0.2. When k_{p2} = 0.2, P_o and Q_o showed low-frequency oscillatory instability with an oscillation frequency of 3.4 Hz. However, when k_{p2} = 0.8, P_o and Q_o showed that the oscillations had been damped and the system was stable. The simulation results were consistent with the theoretical analysis and showed that appropriate increases in the k_{p2} values within a certain range can enhance the stability of grid-forming energy storage systems.

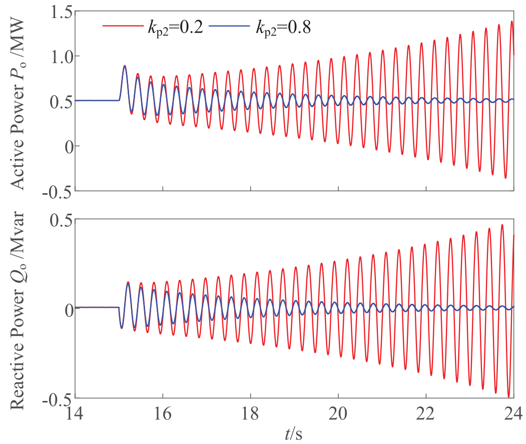

Figure 17: P_o and Q_o response curves at different k_{p2} levels

4.6 Multi-Parameter Coupling Effects on Damping Characteristics

Under a grid strength of 8.2 and an operating condition of 0.5 MW, this paper quantitatively analyzes the influence of the coupling characteristics between the active power-voltage outer-loop proportional coefficient k_{p1} and the reactive power-voltage outer-loop proportional coefficient k_{p2} on the system damping, based on the theoretically derived Eq. (19) and the damping stability criterion. The results are shown in Fig. 18. Fig. 18 illustrates the distribution characteristics of the system damping as k_{p1} and k_{p2} vary. The study reveals that k_{p1} and k_{p2} have a comparable impact on the system damping: when either k_{p1} or k_{p2} increases, the system damping is significantly enhanced; conversely, a decrease in either parameter leads to a corresponding reduction in damping. In particular, when k_{p1} or k_{p2} is set too small, the system damping decreases sharply and exhibits negative damping, thereby inducing oscillatory instability. This finding provides an important theoretical basis for the optimal design of controller parameters in grid-forming energy storage systems, indicating that appropriately increasing both the active power-voltage outer-loop proportional coefficient k_{p1} and the reactive power-voltage outer-loop proportional coefficient k_{p2} contributes to enhanced system damping and improved stability margin.

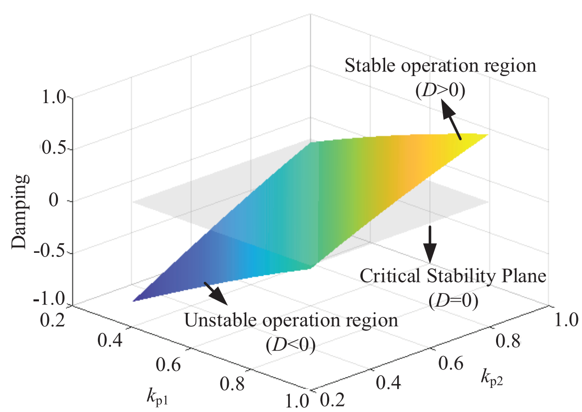

Figure 18: Effect of k_{p1} and k_{p2} variations on system damping

Under a grid strength of 8.2 and an operating condition of 0.5 MW, this paper quantitatively evaluates the influence of coupling between the proportional coefficient k_{p1} and integral coefficient k_{i1} in the active power-voltage outer loop on system damping characteristics, based on the theoretically derived Eq. (19) and the damping stability criterion. The results are shown in Fig. 19, which illustrates the distribution characteristics of system damping with variations in k_{p1} and k_{i1}. The analysis demonstrates that system damping exhibits a significant increasing trend with the rise of either k_{p1} or k_{i1}, whereas damping decreases correspondingly when either parameter is reduced. Particularly, when k_{p1} or k_{i1} is set too small, system damping drops markedly and may even develop negative damping, consequently inducing oscillatory instability. This regularity provides important theoretical guidance for optimizing controller parameters in grid-forming energy storage systems, indicating that appropriate increases in both k_{p1} and k_{i1} contribute to enhanced system damping and improved stability margins.

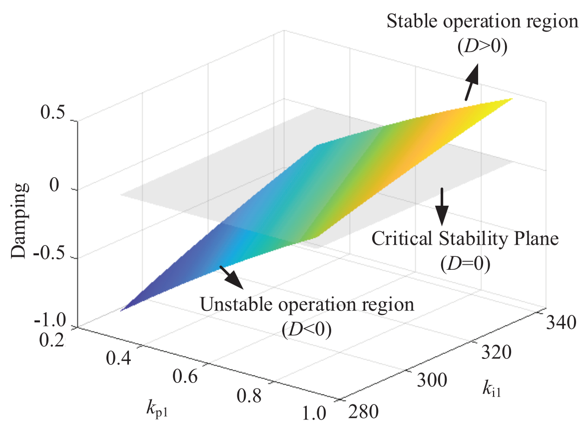

Figure 19: Effect of k_{p1} and k_{i1} variations on system damping

Under a grid strength of 8.2 and an operating condition of 0.5 MW, this paper quantitatively investigates the influence of coupling between the reactive power-voltage regulation coefficient K_q and the voltage droop coefficient K_v on system damping characteristics, based on the theoretically derived Eq. (19) and the damping stability criterion. The results are shown in Fig. 20, which illustrates the distribution characteristics of system damping with variations in K_q and K_v. The findings demonstrate that system damping strengthens with an increase in either K_q or K_v, and weakens with their decrease. Specifically, the voltage droop coefficient K_v exhibits a relatively minor influence on damping, whereas the reactive power-voltage regulation coefficient K_q plays a dominant role in determining system damping. When K_q is sufficiently large, the system consistently maintains positive damping to ensure stable operation. However, when K_q falls below a critical threshold, system damping deteriorates significantly and may even develop negative damping, thereby inducing oscillatory instability. This regularity provides important theoretical guidance for optimizing controller parameters in grid-forming energy storage systems, indicating that prioritizing appropriate K_q values contributes to enhanced system damping and improved stability margins.

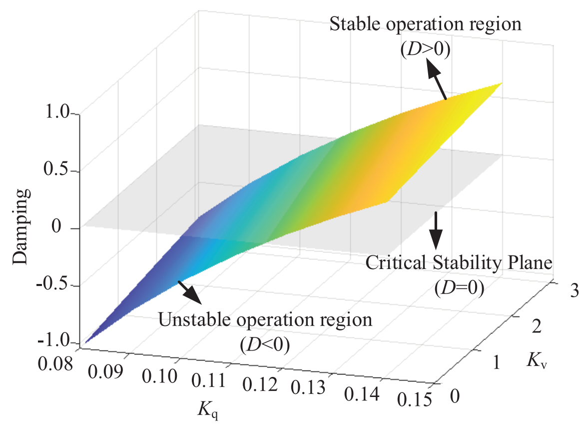

Figure 20: Effect of K_q and K_v variations on system damping

4.7 Advantages over the Existing Solutions

To accurately address low-frequency oscillations, a critical challenge constraining the stable grid integration of grid-forming energy storage systems, and to systematically summarize the characteristics and limitations of existing research methods, Table 9 comprehensively analyzes mainstream research literature and systematically summarizes the advantages and disadvantages of typical methods. Eigenvalue analysis and impedance analysis are two typical methods for studying low-frequency oscillations in grid-forming energy storage systems. The eigenvalue analysis method is based on a detailed state-space model of the system and evaluates system stability by solving the model's eigenvalues. However, the stability information provided by this method is mostly qualitative, making it difficult to precisely quantify the degree of instability of oscillation modes or to reveal the underlying instability mechanisms. The impedance analysis method divides the system into equipment subsystems and grid subsystems, establishes equivalent impedance models for both, and applies the Nyquist criterion for stability discrimination. Although this method has clear physical significance in frequency domain analysis, it struggles to accurately reflect the impact of internal dynamic coupling on stability and cannot intuitively explain the instability mechanism. To overcome the limitations of the above methods, this paper proposes a multi-damping-path model for grid-forming energy storage integration based on the damping torque analysis method. This model simplifies the eighth-order state-space model of the system into a second-order equivalent model, significantly reducing the analytical complexity of low-frequency oscillation problems. Based on the analytical expression of the damping coefficient established in Eq. (19), quantitative evaluation of the influence of control parameters, operating conditions, and grid strength on low-frequency oscillation damping can be achieved.

Table 9: Comparison of research methods

Analysis and research	Advantages	Disadvantages	Ref.
Modal analysis method	1. Provides comprehensive modal characteristic information 2. High accuracy of results 3. Wide applicability	1. Requires detailed system structural parameters 2. Suffers from the "curse of dimensionality" in multi-machine systems 3. High computational complexity	[9–11]

(Continued)

Table 9 (continued)

Analysis and research		Advantages	Disadvantages	Ref.
Impedance analysis method		1. Simple model structure 2. Straightforward derivation process	1. Difficult to accurately characterize the dynamic interaction processes between subsystems	[12–14]
Complex torque analysis method	Embedded torque analysis method	1. Capable of analyzing internal dynamic interaction mechanisms within the system	1. Complex analytical methodology 2. Close coupling among damping paths makes path identification and decoupling difficult	[15]
	Total damping analysis method	1. Simple model structure 2. Straightforward derivation process	1. Unable to effectively reveal internal dynamic interaction mechanisms of the system	[16,17]
	Method proposed in this paper (Multi-Damping-Path Analysis Method)	1. Capable of clearly identifying internal system interaction mechanisms 2. Explicit damping paths enable rapid identification of key instability factors 3. Concise analytical methodology 4. Strong scalability, suitable for multi-machine system analysis	1. The overall derivation process remains relatively complex	/

The constructed model reasonably explains the phenomenon that the system is prone to low-frequency oscillations when grid strength increases but remains stable when grid strength is weak. Research shows that under fixed control parameters, when the grid strength gradually increases to a critical value (7.82 under the conditions set in this paper), the system will enter an unstable state and exhibit low-frequency oscillations. On this basis, this paper further analyzes the influence characteristics of various parameters in the grid-forming energy storage system on stability. The results indicate that, within a certain range, appropriately increasing the active power-voltage outer-loop proportional coefficient k_{p1}, the active power-voltage outer-loop integral coefficient k_{i1}, the reactive power-voltage outer-loop proportional coefficient k_{p2}, and the reactive power-voltage regulation coefficient K_q of the grid-forming energy storage helps enhance system damping and improve the stable operation margin. This study provides a theoretical basis and methodological support for the adaptive adjustment of control parameters in grid-forming energy storage integration systems under different operating conditions and grid strengths.

4.8 Engineering Challenges and Technical Prospects

With the continuous increase in renewable energy penetration, grid-forming energy storage has been identified as a key device for constructing new-type power systems due to its dual potential in enhancing grid flexibility and stability. It not only effectively addresses the integration challenges of renewable energy sources such as wind and solar, meeting multi-timescale power balance requirements, but also provides critically needed rotational inertia and damping support to suppress wide-band oscillations caused by high proportions of power electronic devices.

However, as described in this paper, grid-forming energy storage faces small-signal stability issues under strong grid conditions, particularly low-frequency oscillation risks, which represent a core challenge for its large-scale application. The root cause of this challenge lies in the complex dynamic interaction mechanisms among its internal multiple control loops, making traditional stability analysis methods difficult to accurately quantify the contribution of each control parameter to system damping, resulting in a lack of clear theoretical guidance for parameter setting. The multi-damping torque model proposed in this paper aims to address this challenge, providing basis for optimizing control parameters of grid-forming energy storage from the perspective of damping path decoupling.

From the perspective of engineering application and standardization, grid-forming technology is gradually moving toward standardization. To ensure the safe and stable operation of power systems, various countries have successively issued relevant technical standards. As shown in Table 10, Chinese standards explicitly require that grid-forming equipment must provide effective damping control when the system experiences low-frequency oscillations in the range of 0.2–2.5 Hz with amplitudes greater than 0.003 Hz. This regulation not only imposes mandatory requirements on equipment performance but also demonstrates the practical significance of this paper's research content, namely the accurate analysis of damping characteristics.

Table 10: Damping characteristic standards of various countries

/	**Damping characteristics**
United States	Oscillation active damping is not permitted
Germany	It must pass frequency deviation tests at different frequency points to verify the absence of undamped power oscillations
Finland	On the premise of not reducing the damping of oscillation modes in the 0.2–0.5 Hz range, positive damping must be provided to the power grid between 0–47 Hz and 53–250 Hz
United Kingdom	A natural response to system low-frequency oscillations must be achieved within 5 ms, with the damping coefficient configurable between 0.2 and 5
China	When low-frequency oscillations in the range of 0.2–2.5 Hz occur with oscillation amplitudes exceeding 0.003 Hz, damping control shall be provided. The power response shall be no less than 10% and no greater than 30%, with a response time not less than 0.5 s

The future development of grid-forming energy storage technology depends on the deep integration of "mechanism research" and "engineering application". On one hand, it is necessary to further develop refined analysis methods similar to the multi-damping torque model to reveal oscillation mechanisms under more complex operating conditions. This paper currently focuses only on low-frequency oscillation analysis of single grid-forming energy storage unit grid-connected systems, while small-signal stability analysis for multiple grid-forming energy storage unit grid-connected systems in practical engineering still requires further research. On the other hand, due to limited conditions, this paper suggests that follow-up research should further promote the transformation of these theoretical achievements into parameter setting guidelines and standard testing procedures that are easy to engineering apply, ultimately forming a complete technical chain from modeling, analysis to control, and verification, providing solid support for constructing new-type power systems with high renewable energy penetration.

5 Conclusion

This study addressed the issue of low-frequency oscillations in grid-forming energy storage systems under strong grid conditions. A multi-damping torque model for grid-forming energy storage was constructed, a quantitative analysis of low-frequency oscillation stability was performed at various grid strengths and under different operating conditions and control parameters, and the mechanism associated with the low-frequency oscillations during grid-forming energy storage under strong grid conditions was revealed. The main conclusions are as follows:

(1) A multi-damping torque model for grid-forming energy storage systems was constructed and was used to identify the mechanism associated with low-frequency oscillations in such systems under strong grid conditions. As grid strength increased, the negative damping characteristics significantly intensified. However, the system was unstable and induced low-frequency oscillations when the total system damping became negative.

(2) The impact of operating conditions on the damping characteristics of grid-forming energy storage was quantitatively evaluated. The results showed that grid-forming energy storage was prone to low-frequency oscillation instability under low operating conditions. As the system operating power decreased, the inherent virtual damping of the system often became insufficient to counteract the negative damping components. This resulted in negative total damping, caused system instability, and led to low-frequency oscillations.

(3) The influence of different control parameters on the low-frequency oscillation stability of grid-forming energy storage was quantitatively analyzed. Appropriate increases in the reactive power-voltage regulation coefficient (K_q), the active voltage outer loop proportional coefficient (k_{p1}), the active power-voltage outer-loop integral coefficient (k_{i1}), and the reactive voltage outer loop proportional coefficient (k_{p2}) effectively enhanced the low-frequency oscillation stability of grid-forming energy storage. The results from this study provide theoretical guidance for the tuning of control parameters in grid-forming energy storage systems.

Acknowledgement: We thank International Science Editing (http://www.internationalscienceediting.com, accessed on 01 January 2025) for editing this manuscript.

Funding Statement: This research was funded by Supported by the Science and Technology Project of State Grid Corporation of China (2025220202000070).

Author Contributions: The authors confirm contribution to the paper as follows: Conceptualization—ideas, formulation or evolution of overarching research goals and aims, Qiang Liu and Yongqiang Zhou; Writing—original draft—preparation, creation and/or presentation of the published work, specifically writing the initial draft (including substantive translation), Chaoyang Lu; Writing—review & editing—preparation, creation and/or presentation of the published work by those from the original research group, specifically critical review, commentary or revision—including pre- or post-publication stages, Zhen Yan; Project administration—management and coordination responsibility for the research activity planning and execution, Gangui Yan and Yupeng Wang; Software and validation—oversight and leadership responsibility for the research activity planning and execution, including mentorship external to the core team and verification, whether as a part of the activity or separate, of the overall replication/reproducibility of results/experiments and other research outputs, Cheng Yang. All authors reviewed the results and approved the final version of the manuscript.

Availability of Data and Materials: Not applicable.

Ethics Approval: Not applicable.

Conflicts of Interest: The authors declare no conflicts of interest to report regarding the present study.

Appendix A

The state-space matrix A is shown below:

$$A=\begin{bmatrix} d_1 & d_2 & d_3 & d_4 & d_5 & d_6 & d_7 & d_8 \\ d_9 & d_{10} & 0 & d_{11} & 0 & d_{12} & d_{13} & d_{14} \\ c_1 & c_2 & c_3 & c_4 & c_5 & c_6 & c_7 & c_8 \\ -b_9 & -b_{10} & 0 & -b_{11} & 0 & -b_{12} & -b_{13} & u_{\mathrm{d0}}-b_{14} \\ k_{\mathrm{p1}}c_1-1 & k_{\mathrm{p1}}c_2 & k_{\mathrm{p1}}c_3+k_{\mathrm{i1}} & k_{\mathrm{p1}}c_4 & k_{\mathrm{p1}}c_5 & k_{\mathrm{p1}}c_6 & k_{\mathrm{p1}}c_7 & k_{\mathrm{p1}}c_8 \\ -k_{\mathrm{p2}}b_9 & -k_{\mathrm{p2}}b_{10}-1 & 0 & -k_{\mathrm{p2}}b_{11}+k_{i2} & 0 & -k_{\mathrm{p2}}b_{12} & -k_{\mathrm{p2}}b_{13} & k_{\mathrm{p2}}\left(u_{\mathrm{d0}}-b_{14}\right)+i_{\mathrm{d0}} \\ -\dfrac{1.5b_1i_{\mathrm{d0}}+1.5u_{\mathrm{d0}}}{J} & -\dfrac{1.5b_2i_{\mathrm{d0}}}{J} & -\dfrac{1.5b_3i_{\mathrm{d0}}}{J} & -\dfrac{1.5b_4i_{\mathrm{d0}}}{J} & -\dfrac{1.5b_5i_{\mathrm{d0}}}{J} & -\dfrac{1.5b_6i_{\mathrm{d0}}}{J} & -\dfrac{1.5b_7i_{\mathrm{d0}}+D_{\mathrm{p}}}{J} & -\dfrac{1.5b_8i_{\mathrm{d0}}}{J} \\ 0 & 0 & 0 & 0 & 0 & 0 & 1 & 0 \end{bmatrix}$$

where L_{fg}, a_1–a_{14}, b_1–b_{14}, c_1–c_8, and d_1–d_{14} are shown below:

$$L_{\mathrm{fg}}=\frac{L_{\mathrm{g}}}{L_{\mathrm{f}}+L_{\mathrm{g}}}, \tag{A1}$$

$$\begin{aligned} &a_1=-k_{\mathrm{p3}}k_{\mathrm{p1}}K_{\mathrm{v}}K_{\mathrm{q}}-k_{\mathrm{p3}}k_{\mathrm{p1}}+1,\ a_2=-1.5k_{\mathrm{p3}}k_{\mathrm{p1}}K_{\mathrm{q}}i_{\mathrm{d0}},\ a_3=-k_{\mathrm{p3}},\ a_4=1.5k_{\mathrm{p3}}k_{\mathrm{p1}}K_{\mathrm{q}}u_{\mathrm{d0}}-\omega_0L_{\mathrm{f}},\ a_5=k_{\mathrm{p3}}k_{\mathrm{i1}},\\ &a_6=k_{\mathrm{i3}},\ a_7=\omega_0L_{\mathrm{f}}i_{\mathrm{d0}},\ a_8=-k_{\mathrm{p4}}k_{\mathrm{p2}}+1,\ a_9=\omega_0L_{\mathrm{f}},\ a_{10}=-k_{\mathrm{p4}},\ a_{11}=k_{\mathrm{p4}}k_{\mathrm{i2}},\ a_{12}=k_{\mathrm{i4}},\ a_{13}=L_{\mathrm{f}}i_{\mathrm{d0}},\\ &a_{14}=k_{\mathrm{p4}}k_{\mathrm{p2}}u_{\mathrm{d0}}+k_{\mathrm{p4}}i_{\mathrm{d0}}, \end{aligned} \tag{A2}$$

$$\begin{aligned} &b_1=\frac{L_{\mathrm{fg}}^2a_2a_9+\left(1-L_{\mathrm{fg}}a_8\right)L_{\mathrm{fg}}a_3}{\left(1-L_{\mathrm{fg}}a_8\right)\left(1-L_{\mathrm{fg}}a_1\right)},\ b_2=\frac{L_{\mathrm{fg}}^2a_2a_{10}+\left(1-L_{\mathrm{fg}}a_8\right)L_{\mathrm{fg}}a_4}{\left(1-L_{\mathrm{fg}}a_8\right)\left(1-L_{\mathrm{fg}}a_1\right)},\ b_3=\frac{L_{\mathrm{fg}}a_5}{\left(1-L_{\mathrm{fg}}a_1\right)},\\ &b_4=\frac{L_{\mathrm{fg}}^2a_2a_{11}}{\left(1-L_{\mathrm{fg}}a_8\right)\left(1-L_{\mathrm{fg}}a_1\right)},\ b_5=\frac{L_{\mathrm{fg}}a_6}{\left(1-L_{\mathrm{fg}}a_1\right)},\ b_6=\frac{L_{\mathrm{fg}}^2a_2a_{12}}{\left(1-L_{\mathrm{fg}}a_8\right)\left(1-L_{\mathrm{fg}}a_1\right)},\ b_7=\frac{L_{\mathrm{fg}}^2a_2a_{13}}{\left(1-L_{\mathrm{fg}}a_8\right)\left(1-L_{\mathrm{fg}}a_1\right)},\\ &b_8=\frac{L_{\mathrm{fg}}^2a_2a_{14}+\left(1-L_{\mathrm{fg}}a_8\right)L_{\mathrm{fg}}a_7}{\left(1-L_{\mathrm{fg}}a_8\right)\left(1-L_{\mathrm{fg}}a_1\right)},\ b_9=\frac{L_{\mathrm{fg}}a_9}{1-L_{\mathrm{fg}}a_8},\ b_{10}=\frac{L_{\mathrm{fg}}a_{10}}{1-L_{\mathrm{fg}}a_8},\\ &b_{11}=\frac{L_{\mathrm{fg}}a_{11}}{1-L_{\mathrm{fg}}a_8},\ b_{12}=\frac{L_{\mathrm{fg}}a_{12}}{1-L_{\mathrm{fg}}a_8},\ b_{13}=\frac{L_{\mathrm{fg}}a_{13}}{1-L_{\mathrm{fg}}a_8},\ b_{14}=\frac{L_{\mathrm{fg}}a_{14}}{1-L_{\mathrm{fg}}a_8}, \end{aligned} \tag{A3}$$

$$\begin{aligned} &c_1=\left(-K_{\mathrm{v}}K_{\mathrm{q}}-1\right)b_1-1.5K_{\mathrm{q}}b_9i_{\mathrm{d0}},\ c_2=\left(-K_{\mathrm{v}}K_{\mathrm{q}}-1\right)b_2-1.5K_{\mathrm{q}}b_{10}i_{\mathrm{d0}}+1.5K_{\mathrm{q}}u_{\mathrm{d0}},\ c_3=\left(-K_{\mathrm{v}}K_{\mathrm{q}}-1\right)b_3,\\ &c_4=\left(-K_{\mathrm{v}}K_{\mathrm{q}}-1\right)b_4-1.5K_{\mathrm{q}}b_{11}i_{\mathrm{d0}},\ c_5=\left(-K_{\mathrm{v}}K_{\mathrm{q}}-1\right)b_5,\ c_6=\left(-K_{\mathrm{v}}K_{\mathrm{q}}-1\right)b_6-1.5K_{\mathrm{q}}b_{12}i_{\mathrm{d0}},\\ &c_7=\left(-K_{\mathrm{v}}K_{\mathrm{q}}-1\right)b_7-1.5K_{\mathrm{q}}b_{13}i_{\mathrm{d0}},\ c_8=\left(-K_{\mathrm{v}}K_{\mathrm{q}}-1\right)b_8-1.5K_{\mathrm{q}}b_{14}i_{\mathrm{d0}}, \end{aligned} \tag{A4}$$

$$\begin{aligned} &d_1=\frac{1}{L_{\mathrm{f}}+L_{\mathrm{g}}}\left(a_1b_1+a_2b_9+a_3\right),\ d_2=\frac{1}{L_{\mathrm{f}}+L_{\mathrm{g}}}\left(a_1b_2+a_2b_{10}+a_4\right)+\omega_0,\ d_3=\frac{1}{L_{\mathrm{f}}+L_{\mathrm{g}}}\left(a_1b_3+a_5\right),\\ &d_4=\frac{1}{L_{\mathrm{f}}+L_{\mathrm{g}}}\left(a_1b_4+a_2b_{11}\right),\ d_5=\frac{1}{L_{\mathrm{f}}+L_{\mathrm{g}}}\left(a_1b_5+a_6\right),\ d_6=\frac{1}{L_{\mathrm{f}}+L_{\mathrm{g}}}\left(a_1b_6+a_2b_{12}\right),\\ &d_7=\frac{1}{L_{\mathrm{f}}+L_{\mathrm{g}}}\left(a_1b_7+a_2b_{13}\right),\ d_8=\frac{1}{L_{\mathrm{f}}+L_{\mathrm{g}}}\left(a_1b_8+a_2b_{14}+a_7\right),\ d_9=\frac{1}{L_{\mathrm{f}}+L_{\mathrm{g}}}\left(a_8b_9+a_9\right)-\omega_0, \end{aligned}$$

$$d_{10} = \frac{1}{L_f + L_g}\left(a_8 b_{10} + a_{10}\right), d_{11} = \frac{1}{L_f + L_g}\left(a_8 b_{11} + a_{11}\right), d_{12} = \frac{1}{L_f + L_g}\left(a_8 b_{12} + a_{12}\right),$$
$$d_{13} = \frac{1}{L_f + L_g}\left(a_8 b_{13} + a_{13}\right), d_{14} = \frac{1}{L_f + L_g}\left(a_8 b_{14} + a_{14}\right) \tag{A5}$$

Appendix B

The state-space matrix A_1 is shown below:

$$A_1 = \begin{bmatrix} h_1 & h_2 & 0 & h_3 \\ -f_6 & -f_5 & 0 & -f_4 + u_{d0} \\ h_4/J & h_5/J & -D_p/J & h_6/J \\ 0 & 0 & 1 & 0 \end{bmatrix}$$

where e_1–e_8, f_1–f_6, g_1–g_6, and h_1–h_6 are shown below:

$$e_1 = -\omega_0 L_g k_{p2}, e_2 = \omega_0 L_g i_{d0} + \omega_0 L_g k_{p2} u_{d0}, e_3 = \omega_0 L_g k_{i2}, e_4 = \omega_0 L_g k_{p1} K_v K_q + \omega_0 L_g k_{p1},$$
$$e_5 = 1.5\omega_0 L_g k_{p1} k_{p2} K_q u_{d0} + 1.5\omega_0 L_g K_q k_{p1} i_{d0} + 1,$$
$$e_6 = -1.5\omega_0 L_g k_{p1} K_q u_{d0} i_{d0} - 1.5\omega_0 L_g k_{p1} K_q u_{d0} k_{p2} u_{d0} + \omega_0 L_g i_{q0},$$
$$e_7 = -1.5\omega_0 L_g k_{p1} K_q u_{d0} k_{i2}, e_8 = -\omega_0 L_g k_{i1}, \tag{A6}$$
$$f_1 = \frac{e_6 e_1 - e_5 e_2}{e_5 - e_4 e_1}, f_2 = \frac{e_7 e_1 - e_5 e_3}{e_5 - e_4 e_1}, f_3 = \frac{e_8 e_1}{e_5 - e_4 e_1}, f_4 = \frac{e_6 - e_4 e_2}{e_4 e_1 - e_5}, f_5 = \frac{e_7 - e_4 e_3}{e_4 e_1 - e_5}, f_6 = \frac{e_8}{e_4 e_1 - e_5}, \tag{A7}$$
$$g_1 = -k_{p1} K_v K_q f_1 - k_{p1} f_1 - 1.5 k_{p1} k_{p2} K_q u_{d0} f_4 - 1.5 K_q k_{p1} i_{d0} f_4 + 1.5 k_{p1} K_q u_{d0} i_{d0} + 1.5 k_{p1} K_q u_{d0} k_{p2} u_{d0} - i_{q0},$$
$$g_2 = -k_{p1} K_v K_q f_2 - k_{p1} f_2 - 1.5 k_{p1} k_{p2} K_q u_{d0} f_5 - 1.5 K_q k_{p1} i_{d0} f_5 + 1.5 k_{p1} K_q u_{d0} k_{i2}$$
$$g_3 = -k_{p1} K_v K_q f_3 - k_{p1} f_3 - 1.5 k_{p1} k_{p2} K_q u_{d0} f_6 - 1.5 K_q k_{p1} i_{d0} f_6 + k_{i1}, g_4 = -k_{p2} f_4 + i_{d0} + k_{p2} u_{d0},$$
$$g_5 = -k_{p2} f_5 + k_{i2}, g_6 = -k_{p2} f_6, \tag{A8}$$
$$h_1 = -K_v K_q f_3 - f_3 - 1.5 K_q i_{d0} f_6 + 1.5 u_{d0} K_q g_6, h_2 = -K_v K_q f_2 - f_2 - 1.5 K_q i_{d0} f_5 + 1.5 u_{d0} K_q g_5,$$
$$h_3 = -K_v K_q f_1 - f_1 - 1.5 K_q i_{d0} f_4 + 1.5 u_{d0} K_q g_4, h_4 = -1.5 f_3 i_{d0} - 1.5 u_{d0} g_3, h_5 = -1.5 f_2 i_{d0} - 1.5 u_{d0} g_2,$$
$$h_6 = -1.5 f_1 i_{d0} - 1.5 u_{d0} g_1. \tag{A9}$$

Appendix C

Detailed Derivation of Multi-Damping-Path Analysis

The output power ΔP_o can be expressed as a function of the reduced-order model state variables $\Delta X_1 = [\Delta x_1, \Delta x_2, \Delta\omega, \Delta\theta]$ according to the transfer function block diagram of grid-forming energy storage shown in Fig. A1.

$$\begin{aligned}\Delta P_o = {} & D_p \Delta\omega + \frac{1.5 i_{d0} X_g^2 k_{p2} k_{i1} + 1.5 u_{d0} k_{i1}}{-X_g^2 k_{p1} k_{p2}\left(-K_v K_q - 1\right) + 1.5 K_q k_{p1} X_g\left(k_{p2} u_{d0} + i_{d0}\right) + 1}\Delta x_1 \\ & + \frac{-1.5^2 X_g^2 K_q k_{p1} k_{i2} i_{d0}^2 - 1.5 i_{d0} X_g k_{i2} - 1.5 u_{d0} X_g k_{p1} k_{i2}\left(-K_v K_q - 1\right) + 1.5^2 k_{p1} K_q u_{d0}^2 k_{i2}}{-X_g^2 k_{p1} k_{p2}\left(-K_v K_q - 1\right) + 1.5 K_q k_{p1} X_g\left(k_{p2} u_{d0} + i_{d0}\right) + 1}\Delta x_2 \\ & + \frac{\left(1.5^2 k_{p1} K_q u_{d0}^2 - 1.5^2 X_g^2 i_{d0}^2 K_q k_{p1} i_{d0} - 1.5 i_{d0} X_g - 1.5 u_{d0} X_g k_{p1}\left(-K_v K_q - 1\right)\right)\left(i_{d0} + k_{p2} u_{d0}\right)}{-X_g^2 k_{p1} k_{p2}\left(-K_v K_q - 1\right) + 1.5 K_q k_{p1} X_g\left(k_{p2} u_{d0} + i_{d0}\right) + 1}\Delta\theta.\end{aligned} \tag{A10}$$

The state variables Δx_1, Δx_2, and $\Delta\omega$ need to be expressed in terms of the state variable $\Delta\theta$. The equations for the intermediate state variables Δx_1 and Δx_2 are shown below:

$$\begin{cases} \dfrac{d\Delta x_1}{dt} = \left(-K_{\mathrm{v}}K_{\mathrm{q}} - 1\right)\Delta u_{\mathrm{d}} - 1.5K_{\mathrm{q}}i_{\mathrm{d0}}\Delta u_{\mathrm{q}} + 1.5u_{\mathrm{d0}}K_{\mathrm{q}}\Delta i_{\mathrm{q}} \\ \dfrac{d\Delta x_2}{dt} = -\Delta u_{\mathrm{q}} + u_{\mathrm{d0}}\Delta\theta \end{cases} \Rightarrow \begin{cases} s\Delta x_1 = \left(-K_{\mathrm{v}}K_{\mathrm{q}} - 1\right)\Delta u_{\mathrm{d}} - 1.5K_{\mathrm{q}}i_{\mathrm{d0}}\Delta u_{\mathrm{q}} \\ +1.5u_{\mathrm{d0}}K_{\mathrm{q}}\Delta i_{\mathrm{q}} \\ s\Delta x_2 = -\Delta u_{\mathrm{q}} + u_{\mathrm{d0}}\Delta\theta \end{cases}. \tag{A11}$$

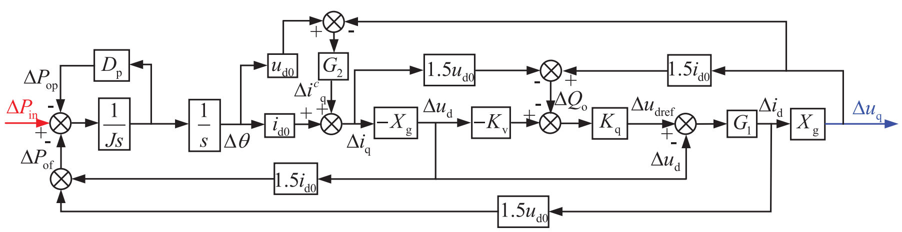

Figure A1: Block diagram of the single input and single output transfer functions for grid-forming energy storage

The state variables Δu_{d}, Δu_{q}, and Δi_{q} need to be derived and expressed in terms of the state variable $\Delta\theta$. The expressions for Δu_{d}, Δu_{q}, Δi_{d}, and Δi_{q} are shown below:

$$\begin{cases} \Delta u_{\mathrm{d}} = -X_{\mathrm{g}}\Delta i_{\mathrm{q}} \\ \Delta u_{\mathrm{q}} = X_{\mathrm{g}}\Delta i_{\mathrm{d}} \end{cases}, \begin{cases} \Delta i_{\mathrm{d}} = -K_{\mathrm{v}}K_{\mathrm{q}}G_1\Delta u_{\mathrm{d}} - 1.5K_{\mathrm{q}}i_{\mathrm{d0}}G_1\Delta u_{\mathrm{q}} + 1.5u_{\mathrm{d0}}K_{\mathrm{q}}G_1\Delta i_{\mathrm{q}} - G_1\Delta u_{\mathrm{d}} \\ \Delta i_{\mathrm{q}} = \left(u_{\mathrm{d0}}G_2 + i_{\mathrm{d0}}\right)\Delta\theta - \Delta u_{\mathrm{q}}G_2 \end{cases}, \tag{A12}$$

where $X_{\mathrm{g}} = \omega_0 L_{\mathrm{g}}$, $G_1 = k_{\mathrm{p1}} + k_{\mathrm{i1}}/s$, $G_2 = k_{\mathrm{p2}} + k_{\mathrm{i2}}/s$.

According to Eq. (A12), the relationship between Δu_{d} and Δu_{q} can be expressed as follows:

$$\Delta u_{\mathrm{q}} = \frac{\left(-K_{\mathrm{v}}K_{\mathrm{q}}X_{\mathrm{g}} - 1.5u_{\mathrm{d0}}K_{\mathrm{q}} - X_{\mathrm{g}}\right)G_1}{1 + 1.5K_{\mathrm{q}}i_{\mathrm{d0}}X_{\mathrm{g}}G_1}\Delta u_{\mathrm{d}}. \tag{A13}$$

According to Eqs. (A12) and (A13), the relationship between the state variable Δu_{d} and the state variable $\Delta\theta$ can be expressed as follows:

$$\Delta u_{\mathrm{d}} = \frac{u_{\mathrm{d0}}X_{\mathrm{g}}G_2 + i_{\mathrm{d0}}X_{\mathrm{g}} + 1.5K_{\mathrm{q}}u_{\mathrm{d0}}i_{\mathrm{d0}}X_{\mathrm{g}}^2G_1G_2 + 1.5K_{\mathrm{q}}i_{\mathrm{d0}}^2X_{\mathrm{g}}^2G_1}{\left(\left(-K_{\mathrm{v}}K_{\mathrm{q}} - 1\right)X_{\mathrm{g}}^2 - 1.5u_{\mathrm{d0}}K_{\mathrm{q}}X_{\mathrm{g}}\right)G_1G_2 - 1.5K_{\mathrm{q}}i_{\mathrm{d0}}X_{\mathrm{g}}G_1 - 1}\Delta\theta = G_{\mathrm{ud}}(s)\,\Delta\theta, \tag{A14}$$

where $G_{\mathrm{ud}}(s)$ represents the transfer function from $\Delta\theta$ to Δu_{d}, and its specific expression is shown below:

$$G_{\mathrm{ud}}(s) = \frac{u_{\mathrm{d0}}X_{\mathrm{g}}G_2 + i_{\mathrm{d0}}X_{\mathrm{g}} + 1.5K_{\mathrm{q}}u_{\mathrm{d0}}i_{\mathrm{d0}}X_{\mathrm{g}}^2G_1G_2 + 1.5K_{\mathrm{q}}i_{\mathrm{d0}}^2X_{\mathrm{g}}^2G_1}{\left(\left(-K_{\mathrm{v}}K_{\mathrm{q}} - 1\right)X_{\mathrm{g}}^2 - 1.5u_{\mathrm{d0}}K_{\mathrm{q}}X_{\mathrm{g}}\right)G_1G_2 - 1.5K_{\mathrm{q}}i_{\mathrm{d0}}X_{\mathrm{g}}G_1 - 1}. \tag{A15}$$

According to Eqs. (A12)–(A14), the relationships between the state variables Δi_{q} and Δu_{q} and the state variable $\Delta\theta$ can be expressed as follows:

$$\begin{cases} \Delta u_{\mathrm{q}} = \dfrac{\left(\left(-K_{\mathrm{v}}K_{\mathrm{q}}-1\right)u_{\mathrm{d0}}X_{\mathrm{g}}^{2}-1.5u_{\mathrm{d0}}^{2}K_{\mathrm{q}}X_{\mathrm{g}}\right)G_1G_2+\left(\left(-K_{\mathrm{v}}K_{\mathrm{q}}-1\right)i_{\mathrm{d0}}X_{\mathrm{g}}^{2}-1.5u_{\mathrm{d0}}i_{\mathrm{d0}}K_{\mathrm{q}}X_{\mathrm{g}}\right)G_1}{\left(\left(-K_{\mathrm{v}}K_{\mathrm{q}}-1\right)X_{\mathrm{g}}^{2}-1.5u_{\mathrm{d0}}K_{\mathrm{q}}X_{\mathrm{g}}\right)G_1G_2-1.5K_{\mathrm{q}}i_{\mathrm{d0}}X_{\mathrm{g}}G_1-1}\Delta\theta = G_{\mathrm{uq}}\left(s\right)\Delta\theta \\ \Delta i_{\mathrm{q}} = -\dfrac{u_{\mathrm{d0}}G_2+i_{\mathrm{d0}}+1.5K_{\mathrm{q}}u_{\mathrm{d0}}i_{\mathrm{d0}}X_{\mathrm{g}}G_1G_2+1.5K_{\mathrm{q}}i_{\mathrm{d0}}^{2}X_{\mathrm{g}}G_1}{\left(\left(-K_{\mathrm{v}}K_{\mathrm{q}}-1\right)X_{\mathrm{g}}^{2}-1.5u_{\mathrm{d0}}K_{\mathrm{q}}X_{\mathrm{g}}\right)G_1G_2-1.5K_{\mathrm{q}}i_{\mathrm{d0}}X_{\mathrm{g}}G_1-1}\Delta\theta = G_{\mathrm{iq}}\left(s\right)\Delta\theta \end{cases}, \tag{A16}$$

where $G_{\mathrm{uq}}(s)$ represents the transfer function from $\Delta\theta$ to Δu_{q}; and $G_{\mathrm{iq}}(s)$ represents the transfer function from $\Delta\theta$ to Δi_{q}. The specific expressions for $G_{\mathrm{uq}}(s)$ and $G_{\mathrm{iq}}(s)$ are given below:

$$\begin{cases} G_{\mathrm{uq}}\left(s\right) = \dfrac{\left(\left(-K_{\mathrm{v}}K_{\mathrm{q}}-1\right)u_{\mathrm{d0}}X_{\mathrm{g}}^{2}-1.5u_{\mathrm{d0}}^{2}K_{\mathrm{q}}X_{\mathrm{g}}\right)G_1G_2+\left(\left(-K_{\mathrm{v}}K_{\mathrm{q}}-1\right)i_{\mathrm{d0}}X_{\mathrm{g}}^{2}-1.5u_{\mathrm{d0}}i_{\mathrm{d0}}K_{\mathrm{q}}X_{\mathrm{g}}\right)G_1}{\left(\left(-K_{\mathrm{v}}K_{\mathrm{q}}-1\right)X_{\mathrm{g}}^{2}-1.5u_{\mathrm{d0}}K_{\mathrm{q}}X_{\mathrm{g}}\right)G_1G_2-1.5K_{\mathrm{q}}i_{\mathrm{d0}}X_{\mathrm{g}}G_1-1} \\ G_{\mathrm{iq}}\left(s\right) = -\dfrac{u_{\mathrm{d0}}G_2+i_{\mathrm{d0}}+1.5K_{\mathrm{q}}u_{\mathrm{d0}}i_{\mathrm{d0}}X_{\mathrm{g}}G_1G_2+1.5K_{\mathrm{q}}i_{\mathrm{d0}}^{2}X_{\mathrm{g}}G_1}{\left(\left(-K_{\mathrm{v}}K_{\mathrm{q}}-1\right)X_{\mathrm{g}}^{2}-1.5u_{\mathrm{d0}}K_{\mathrm{q}}X_{\mathrm{g}}\right)G_1G_2-1.5K_{\mathrm{q}}i_{\mathrm{d0}}X_{\mathrm{g}}G_1-1} \end{cases}. \tag{A17}$$

According to Eqs. (A14) and (A16), Eq. (A11) can be transformed into:

$$\begin{cases} \Delta x_1 = \left(-K_{\mathrm{v}}K_{\mathrm{q}}-1\right)\dfrac{G_{\mathrm{ud}}\left(s\right)}{s}\Delta\theta-1.5K_{\mathrm{q}}i_{\mathrm{d0}}\dfrac{G_{\mathrm{uq}}\left(s\right)}{s}\Delta\theta+1.5u_{\mathrm{d0}}K_{\mathrm{q}}\dfrac{G_{\mathrm{iq}}\left(s\right)}{s}\Delta\theta \\ \Delta x_2 = -G_{\mathrm{uq}}\left(s\right)\dfrac{\Delta\theta}{s}+u_{\mathrm{d0}}\dfrac{\Delta\theta}{s} \end{cases}. \tag{A18}$$

Substituting Eq. (A18) into Eq. (A10) yields:

$$\begin{aligned} \Delta P_{\mathrm{o}} = {} & D_{\mathrm{p}}\Delta\omega+\frac{\left(1.5^2k_{\mathrm{p1}}K_{\mathrm{q}}u_{\mathrm{d0}}^{2}-1.5^2X_{\mathrm{g}}^{2}K_{\mathrm{q}}k_{\mathrm{p1}}i_{\mathrm{d0}}^{2}-1.5i_{\mathrm{d0}}X_{\mathrm{g}}-1.5u_{\mathrm{d0}}X_{\mathrm{g}}k_{\mathrm{p1}}\left(-K_{\mathrm{v}}K_{\mathrm{q}}-1\right)\right)\left(k_{\mathrm{p2}}u_{\mathrm{d0}}+i_{\mathrm{d0}}\right)}{-X_{\mathrm{g}}^{2}k_{\mathrm{p1}}k_{\mathrm{p2}}\left(-K_{\mathrm{v}}K_{\mathrm{q}}-1\right)+1.5K_{\mathrm{q}}k_{\mathrm{p1}}X_{\mathrm{g}}\left(k_{\mathrm{p2}}u_{\mathrm{d0}}+i_{\mathrm{d0}}\right)+1}\Delta\theta \\ & +\frac{-1.5^2X_{\mathrm{g}}^{2}K_{\mathrm{q}}k_{\mathrm{p1}}k_{\mathrm{i2}}u_{\mathrm{d0}}i_{\mathrm{d0}}^{2}-1.5X_{\mathrm{g}}k_{\mathrm{i2}}u_{\mathrm{d0}}i_{\mathrm{d0}}-1.5X_{\mathrm{g}}k_{\mathrm{p1}}k_{\mathrm{i2}}\left(-K_{\mathrm{v}}K_{\mathrm{q}}-1\right)u_{\mathrm{d0}}^{2}+1.5^2K_{\mathrm{q}}k_{\mathrm{p1}}k_{\mathrm{i2}}u_{\mathrm{d0}}^{3}}{-X_{\mathrm{g}}^{2}k_{\mathrm{p1}}k_{\mathrm{p2}}\left(-K_{\mathrm{v}}K_{\mathrm{q}}-1\right)+1.5K_{\mathrm{q}}k_{\mathrm{p1}}X_{\mathrm{g}}\left(k_{\mathrm{p2}}u_{\mathrm{d0}}+i_{\mathrm{d0}}\right)+1}\frac{1}{s}\Delta\theta \\ & +\frac{\left(1.5i_{\mathrm{d0}}X_{\mathrm{g}}^{2}k_{\mathrm{p2}}k_{\mathrm{i1}}+1.5u_{\mathrm{d0}}k_{\mathrm{i1}}\right)\left(-K_{\mathrm{v}}K_{\mathrm{q}}-1\right)}{-X_{\mathrm{g}}^{2}k_{\mathrm{p1}}k_{\mathrm{p2}}\left(-K_{\mathrm{v}}K_{\mathrm{q}}-1\right)+1.5K_{\mathrm{q}}k_{\mathrm{p1}}X_{\mathrm{g}}\left(k_{\mathrm{p2}}u_{\mathrm{d0}}+i_{\mathrm{d0}}\right)+1}\frac{G_{\mathrm{ud}}\left(s\right)}{s}\Delta\theta \\ & +\frac{1.5^2X_{\mathrm{g}}^{2}K_{\mathrm{q}}i_{\mathrm{d0}}^{2}\left(k_{\mathrm{p1}}k_{\mathrm{i2}}-k_{\mathrm{p2}}k_{\mathrm{i1}}\right)-1.5^2K_{\mathrm{q}}k_{\mathrm{i1}}u_{\mathrm{d0}}i_{\mathrm{d0}}+1.5X_{\mathrm{g}}k_{\mathrm{i2}}i_{\mathrm{d0}}+1.5X_{\mathrm{g}}k_{\mathrm{p1}}k_{\mathrm{i2}}u_{\mathrm{d0}}\left(-K_{\mathrm{v}}K_{\mathrm{q}}-1\right)-1.5^2K_{\mathrm{q}}k_{\mathrm{p1}}k_{\mathrm{i2}}u_{\mathrm{d0}}^{2}}{-X_{\mathrm{g}}^{2}k_{\mathrm{p1}}k_{\mathrm{p2}}\left(-K_{\mathrm{v}}K_{\mathrm{q}}-1\right)+1.5K_{\mathrm{q}}k_{\mathrm{p1}}X_{\mathrm{g}}\left(k_{\mathrm{p2}}u_{\mathrm{d0}}+i_{\mathrm{d0}}\right)+1}\frac{G_{\mathrm{uq}}\left(s\right)}{s}\Delta\theta \\ & +\frac{1.5^2X_{\mathrm{g}}^{2}K_{\mathrm{q}}k_{\mathrm{p2}}k_{\mathrm{i1}}u_{\mathrm{d0}}i_{\mathrm{d0}}+1.5^2K_{\mathrm{q}}k_{\mathrm{i1}}u_{\mathrm{d0}}^{2}}{-X_{\mathrm{g}}^{2}k_{\mathrm{p1}}k_{\mathrm{p2}}\left(-K_{\mathrm{v}}K_{\mathrm{q}}-1\right)+1.5K_{\mathrm{q}}k_{\mathrm{p1}}X_{\mathrm{g}}\left(k_{\mathrm{p2}}u_{\mathrm{d0}}+i_{\mathrm{d0}}\right)+1}\frac{G_{\mathrm{iq}}\left(s\right)}{s}\Delta\theta. \end{aligned} \tag{A19}$$

Transforming Eq. (A20) yields:

$$\Delta P_{\mathrm{o}} = D_{\mathrm{p}}\Delta\omega+\left(K_1+\frac{K_2}{s}\right)\Delta\theta+\frac{K_3}{s}\Delta u_{\mathrm{d}}+\frac{K_4}{s}\Delta u_{\mathrm{q}}+\frac{K_5}{s}\Delta i_{\mathrm{q}}, \tag{A20}$$

where K_1–K_5 are:

$$\begin{cases} K_1 = \dfrac{\left(1.5^2 k_{p1} K_q u_{d0}^2 - 1.5^2 X_g^2 K_q k_{p1} i_{d0}^2 - 1.5 i_{d0} X_g - 1.5 u_{d0} X_g k_{p1}\left(-K_v K_q - 1\right)\right)\left(k_{p2} u_{d0} + i_{d0}\right)}{-X_g^2 k_{p1} k_{p2}\left(-K_v K_q - 1\right) + 1.5 K_q k_{p1} X_g\left(k_{p2} u_{d0} + i_{d0}\right) + 1} \\ K_2 = \dfrac{-1.5^2 X_g^2 K_q k_{p1} k_{i2} u_{d0} i_{d0}^2 - 1.5 X_g k_{i2} u_{d0} i_{d0} - 1.5 X_g k_{p1} k_{i2}\left(-K_v K_q - 1\right) u_{d0}^2 + 1.5^2 K_q k_{p1} k_{i2} u_{d0}^3}{-X_g^2 k_{p1} k_{p2}\left(-K_v K_q - 1\right) + 1.5 K_q k_{p1} X_g\left(k_{p2} u_{d0} + i_{d0}\right) + 1} \\ K_3 = \dfrac{\left(1.5 i_{d0} X_g^2 k_{p2} k_{i1} + 1.5 u_{d0} k_{i1}\right)\left(-K_v K_q - 1\right)}{-X_g^2 k_{p1} k_{p2}\left(-K_v K_q - 1\right) + 1.5 K_q k_{p1} X_g\left(k_{p2} u_{d0} + i_{d0}\right) + 1} \\ K_4 = \dfrac{1.5^2 X_g^2 K_q i_{d0}^2\left(k_{p1} k_{i2} - k_{p2} k_{i1}\right) - 1.5^2 K_q k_{i1} u_{d0} i_{d0} + 1.5 X_g k_{i2} i_{d0} + 1.5 X_g k_{p1} k_{i2} u_{d0}\left(-K_v K_q - 1\right) - 1.5^2 K_q k_{p1} k_{i2} u_{d0}^2}{-X_g^2 k_{p1} k_{p2}\left(-K_v K_q - 1\right) + 1.5 K_q k_{p1} X_g\left(k_{p2} u_{d0} + i_{d0}\right) + 1} \\ K_5 = \dfrac{1.5^2 X_g^2 K_q k_{p2} k_{i1} u_{d0} i_{d0} + 1.5^2 K_q k_{i1} u_{d0}^2}{-X_g^2 k_{p1} k_{p2}\left(-K_v K_q - 1\right) + 1.5 K_q k_{p1} X_g\left(k_{p2} u_{d0} + i_{d0}\right) + 1} \end{cases} . \tag{A21}$$

References

1. Leite R, Oleskkovicz M. The joint application of photovoltaic generation and distributed or concentrated energy storage systems in a low voltage distribution network: a case study. IEEE Lat Am Trans. 2023;21(10):1122–31. doi:10.1109/tla.2023.10255443.
2. Kittner N, Lill F, Kammen DM. Energy storage deployment and innovation for the clean energy transition. Nat Energy. 2017;2(9):17125. doi:10.1038/nenergy.2017.125.
3. Zheng Y, Han Y, Wang C, Ren Q, Yang P, Zalhaf AS. Impact of phase-locked loop on grid-connected inverter stability under weak grid conditions and suppression measures. Comput Electr Eng. 2025;123(12):110249. doi:10.1016/j.compeleceng.2025.110249.
4. Johnson BB, Dhople SV, Hamadeh AO, Krein PT. Synchronization of parallel single-phase inverters with virtual oscillator control. IEEE Trans Power Electron. 2014;29(11):6124–38. doi:10.1109/tpel.2013.2296292.
5. Qi Y, Che Y, Liu L, Ni J, Zhang S. Optimization configuration method for grid-side grid-forming energy storage system based on genetic algorithm. Energy Eng. 2025;1–10. doi:10.32604/ee.2025.068054.
6. Zhao C, Chai W, Rui B, Chen L. Analysis of sub-synchronous oscillation of virtual synchronous generator and research on suppression strategy in weak grid. Energy Eng. 2023;120(11):2683–705. doi:10.32604/ee.2023.029620.
7. Zhu Q, Guo D, Ruan R, Chai Z, Wang C, Guan Z. The emergency control method for multi-scenario sub-synchronous oscillation in wind power grid integration systems based on transfer learning. Energy Eng. 2025;122(8):3133–54. doi:10.32604/ee.2025.063165.
8. Salem Q, Fawaz BB, Aljarrah R, Karimi M. Grid forming converters for low inertia systems-capabilities and limitations: a critical review. IEEE Open J Ind Electron Soc. 2025;6:775–801. doi:10.1109/OJIES.2025.3566213.
9. Ali SA, Serna-Torre P, Hidalgo-Gonzalez P, Dozein MG, Bahrani B. Modularized small-signal modeling of grid-forming inverters. IEEE Access. 2025;13(18):97011–37. doi:10.1109/ACCESS.2025.3572689.
10. Zhao F, Wang X, Zhou Z, Harnefors L, Svensson JR, Kocewiak Ł.H, et al. Control interaction modeling and analysis of grid-forming battery energy storage system for offshore wind power plant. IEEE Trans Power Syst. 2022;37(1):497–507. doi:10.1109/TPWRS.2021.3096850.
11. Liu K, Qian T, Zhang W, Wu S, Han R, Hou K, et al. Review on small-signal stability of multiple virtual synchronous generators. Renew Sustain Energy Rev. 2025;215(22):115543. doi:10.1016/j.rser.2025.115543.
12. Jin X, Wang J, Yan H, Ni X, Ji Z, Ji B, et al. Series-parallel sequence impedance models of multi-loop grid-forming converters. J Mod Power Syst Clean Energy. 2024;13(1):29–41. doi:10.35833/mpce.2024.000676.
13. Liu N, Wang H, Sun L, Zhou W, Song J, Zhou D, et al. Modular impedance modeling and stability analysis of hybrid AC/DC power systems with grid-forming and grid-following converters. IEEE Access. 2024;12:4063–77. doi:10.1109/ACCESS.2023.3348784.

14. Narula A, Bongiorno M, Mattavelli P, Beza M, Svensson JR, Liu W. Evaluation and comparison of small-signal characteristics of grid-forming converter systems in two different reference frames. IEEE Open J Ind Appl. 2025;6:206–20. doi:10.1109/ojia.2025.3564501.
15. Zhou Y, Li S, Li Y, Qin L, Sun H, Wu J, et al. Structure-preserving stability analysis of multi-loop virtual synchronous machine based on chimeric torque method. Power Syst Technol. 2022;46(2):733–51. (In Chinese). doi:10.13335/j.1000-3673.pst.2021.1334.
16. Zhou Z, Pugliese S, Langwasser M, Liserre M. Sub-synchronous damping by battery storage system in grid forming control mode. In: 2022 IEEE Energy Conversion Congress and Exposition (ECCE); 2022 Oct 9–13. Detroit, MI, USA. p. 1–8. doi:10.1109/ECCE50734.2022.9947758.
17. Zhang K, Shi M, Chen X, Shao D, Xu Y, Chen Y. Interaction modeling and stability analysis of grid-forming energy storage system based on SISO transfer functions. IEEE Trans Sustain Energy. 2025;16(1):573–87. doi:10.1109/tste.2024.3471801.
18. Demello F, Concordia C. Concepts of synchronous machine stability as affected by excitation control. IEEE Trans Power Apparatus Syst. 1969;PAS-88(4):316–29. doi:10.1109/tpas.1969.292452.